IOWA STATE UNIVERSITY
Digital Repository

Graduate Theses and Dissertations

Iowa State University Capstones, Theses and Dissertations

2013

Quantitative flaw characterization with ultrasonic phased arrays

Brady Engle
Iowa State University

Follow this and additional works at: https://lib.dr.iastate.edu/etd

 Part of the Acoustics, Dynamics, and Controls Commons, and the Aerospace Engineering Commons

Recommended Citation
Engle, Brady, "Quantitative flaw characterization with ultrasonic phased arrays" (2013). *Graduate Theses and Dissertations*. 13127.
https://lib.dr.iastate.edu/etd/13127

This Thesis is brought to you for free and open access by the Iowa State University Capstones, Theses and Dissertations at Iowa State University Digital Repository. It has been accepted for inclusion in Graduate Theses and Dissertations by an authorized administrator of Iowa State University Digital Repository. For more information, please contact digirep@iastate.edu.

www.manaraa.com

Quantitative flaw characterization with ultrasonic phased arrays

by

Brady John Engle

A thesis submitted to the graduate faculty

in partial fulfillment of the requirements for the degree of

MASTER OF SCIENCE

Major: Engineering Mechanics

Program of Study Committee:

Lester W. Schmerr, Jr., Major Professor

Timothy A. Gray

Thomas J. Rudolphi

Iowa State University

Ames, Iowa

2013

Copyright © Brady John Engle, 2013. All rights reserved.

www.manaraa.com

TABLE OF CONTENTS

www.manaraa.com

www.manaraa.com

LIST OF TABLES

www.manaraa.com

LIST OF FIGURES

www.manaraa.com

www.manaraa.com

www.manaraa.com

ACKNOWLEDGEMENTS

This work was supported by the National Science Foundation Industry/University Cooperative Research Center program at the Center for Nondestructive Evaluation, Iowa State University.

www.manaraa.com

ABSTRACT

Ultrasonic nondestructive evaluation (NDE) is a critical diagnostic tool in many industries. It is used to characterize potentially dangerous flaws in critical components for aerospace, automotive, and energy applications. The use of phased array transducers allows for the extension of traditional techniques and the introduction of new methods for quantitative flaw characterization. An equivalent flaw sizing technique for use in time-of-flight diffraction setups is presented that provides an estimate of the size and orientation of isolated cracks, surface-breaking cracks, and volumetric flaws such as voids and inclusions. Experimental validation is provided for the isolated crack case. A quantitative imaging algorithm is developed that corrects for system effects and wave propagation, making the images formed directly related to the properties of the scatterer present. Simulated data is used to form images of cylindrical and spherical inclusions. The contributions of different signals to the image formation process are discussed and examples of the quantitative nature of the images are shown.

www.manaraa.com

CHAPTER 1. GENERAL INTRODUCTION

Introduction

Background

Ultrasound is widely used as a diagnostic tool in the aerospace, automotive, nuclear, and oil/gas industries as well as in medicine. In the medical field, it is estimated that one quarter of all diagnostic images are made using ultrasound [1]. In industry, the use of ultrasound is termed ultrasonic nondestructive evaluation (NDE) and is used to identify and characterize defects in critical components.

An ultrasonic inspection is traditionally carried out with a piezoelectric transducer to transmit a sound wave into the material being inspected and using either the same transducer or a second transducer to receive some scattered or transmitted form of that sound wave. Using the same transducer in transmission and reception is referred to as pulse-echo, while using different transducers is called pitch-catch. The transmission process occurs by applying a voltage across the piezoelectric element of the transducer, which creates a mechanical wave. The reception process is the reverse of this; a mechanical wave impinges on the piezoelectric element generating a voltage which can be measured and displayed as a function of time. Such displays of received voltage as a function of time are often referred to as waveforms or A-scans. When the sound wave inside the material encounters changes in material properties, such as wave speed and density, some of the sound energy will be scattered, reflected, or refracted. Changes in material properties could be caused by cracks, voids, inclusions, or other flaws for NDE applications and by changes in body tissue types – such as the presence of tumors – in

www.manaraa.com

the medical field. The ultimate goal of an ultrasonic inspection is to use the measured voltage from the receiving transducer to infer what types of scattering features are present in the test material.

A-scans can show the times at which certain features are detected as well as their relative amplitudes, but generally it is difficult to get a good understanding of what is being seen just by looking at unprocessed A-scans. Using the information contained in the A-scans, images can be made to visualize the data in ways that better lend themselves to feature identification. Ultrasonic imaging is an umbrella term for a wide variety of techniques that use some form of processing to display A-scan data in ways that improve feature identification. Several types of imaging are frequently used in both NDE and medical applications. To form images multiple A-scans must be collected. This is usually done by performing a raster scan or by sweeping the angle of the transducer. B-scans use multiple A-scans side-by-side to display a two-dimensional plot of voltage amplitude as a function of scan position and time, which can be thought of as depth. Sector scans (S-scans) are a type of B-scan where the scan dimension is the transducer angle. C-scans are 2-D plots showing some voltage value of interest formed by performing a 2-D scan of the transducer over an area. A common choice of voltage value is to look for the maximum voltage within a specific time range. The resulting C-scan would then be a 2-D plot of that maximum voltage value as a function of the two scan dimensions. Different images may be used depending on the inspection type. In the medical field, for example, objects being imaged often have some dependency on time which means the data acquisition and display must be fast enough to capture this behavior. However, many NDE applications have no time-dependence, which means that scans can take longer and the data would not need to be viewed in real-time.

Imaging is not the only way that information about flaws and defects can be obtained in NDE inspections. One can also use models to infer flaw characteristics from a relatively small number of A-scans. Equivalent flaw sizing is an example of such a model-based approach where the size and orientation of an unknown flaw are obtained in terms of a best fit simple

www.manaraa.com

shape such as an ellipse or ellipsoid [2]. This thesis will examine both imaging and model-based approaches to flaw characterization using phased arrays.

Phased arrays

Phased array transducers differ from traditional single-element transducers in that they have multiple piezoelectric elements that operate independently of each other. Any combination of elements can be used in either transmission or reception, and amplitude weights and time delays can be applied to each element individually. Different sets of weights and time delays applied to the elements of an array are called apodization laws and delay laws, respectively. Array elements are typically small enough to be considered point sources that propagate widely-spreading spherical waves, whereas larger single-element transducers propagate a highly directional (i.e. well-collimated) beam of sound. If all the elements of an array are used with no time delays, the spherical waves from each individual element will combine to form a single wave front that is similar to that of a single-element transducer of size equal to that of the overall array. However, if the appropriate time delays are chosen, those spherical waves can combine to produce a steered beam, a focused beam, or a combination of both.

The ability of arrays to steer, focus, and otherwise tailor their sound beams allows them to often outperform single-element transducers in the formation of images. Mechanical scanning, for example, can be replaced with electronic steering in many cases, leading to more rapid inspections.

In addition to having improved capabilities to form the same types of images generated with single-element transducers, arrays allow for advanced imaging algorithms to be developed that are physically impossible with single-element transducers. This is possible since one can send and receive on all the potential pairs of elements present in an array and use that capability to form up images of various combinations of responses.

The ability of arrays to steer their sound beams also makes arrays potentially valuable for conducting model-based approaches where the waves scattered from a flaw in a number of

www.manaraa.com

directions are used to infer flaw size. Equivalent flaw sizing, as mentioned previously, is an example of such a model-based approach. Time-of-flight diffraction (TOFD) sizing is another [3]. For both of these methods the ability of an array to obtain flaw responses at different "look-angles" allows them to efficiently replace multiple traditional single-element setups.

Scope of the thesis

This work will focus on the development and implementation of methods and algorithms to detect and quantitatively characterize flaws and defects in NDE applications using the unique properties of ultrasonic phased array transducers. There will be two parts to this thesis. First, a flaw sizing method will be developed that will adapt an equivalent flaw sizing method originally developed for single-element transducer inspections to phased arrays, leading to a more effective and practical inspection. This method will be demonstrated with both simulated and experimental data. One important application of this method includes weld inspections, where flaw size is needed to determine the fitness of the weld for service. Second, a new quantitative phased array imaging algorithm will be presented that defines explicitly the nature of the flaw image in terms of the physical properties of the flaw. To test this imaging method and to study the image formation process in detail, a software-based "test bed" has been developed which will be used to analyze images of cylindrical and spherical inclusions using simulated data. The detection and characterization of inclusions is important in a number of industries. In the aircraft engine industry, for example, brittle hard alpha inclusions in titanium act as starting points for fatigue cracks and can lead to catastrophic failure, such as in the rupture of an engine of United Airlines Flight 232 which crashed in Sioux City, IA in 1989.

Literature Review

There are a number of areas that can be considered the foundation for this work where a review of the relevant literature is necessary. In the case of flaw sizing (the topic of Chapter 2)

www.manaraa.com

brief reviews of the history of the time-of-flight diffraction (TOFD) and equivalent flaw sizing methods are given. For imaging (the topic of Chapter 3) a short summary is given of the current state of phased array imaging, and the history of the physical optics far-field inverse scattering (POFFIS) method [4], which is closely related to the new imaging approach, is discussed.

Time-of-flight diffraction sizing

It is common practice in NDE testing to size flaws by scanning a single-element transducer over a flaw and recording the extent over which the amplitude of the flaw signal is significant. This method is called the dB drop method. However, this method is not useful for sizing flaws smaller than the size of the transducer and has poor reliability [5]. Time-of-flight diffraction (TOFD) sizing was developed by Silk at the National Nondestructive Testing Center in Harwell, England, in the 1970s to provide an alternative method for sizing flaws such as cracks. The method identifies the waves scattered from the tips of a crack and uses the time-of-flight between those tips to estimate the length of the crack. Today TOFD sizing is widely used in industrial applications, and Charlesworth and Temple provide a thorough overview of the method in their book [3].

Equivalent flaw sizing

The TOFD method provides a measure of the size of a crack in terms of a single length parameter. In reality cracks have multiple dimensions and this information is useful in modern reliability evaluations that use fracture mechanics. Equivalent flaw sizing is a model-based approach that attempts to size a flaw in terms of a simple equivalent flaw shape such as an ellipse or ellipsoid. To obtain the information needed to construct such equivalent shapes, one needs to interrogate the flaw from multiple directions. Equivalent flaw sizing has its roots in the work of Rose using inverse Born approximation sizing [6]. This early work used a specially designed multi-viewing transducer system and a non-linear optimization algorithm to estimate flaw size and orientation [7]. In 1992 Chiou and Schmerr introduced a linear least

www.manaraa.com

squares/eigenvalue method for the equivalent flaw sizing of cracks and volumetric flaws using backscatter data from a relatively small number of incident wave directions [8]. This method made the determination of the equivalent flaw parameters simpler and more robust but still required precise mechanical scanning/orientation of single-element transducers, making the method costly and often difficult to implement. It will be shown in Chapter 2 that phased arrays give equivalent flaw sizing a new lease on life by making it much easier to acquire the needed data.

Phased array imaging

As mentioned previously, phased array transducers allow for the formation of images that would not be possible with single-element transducers. This is because A-scans can be obtained for every possible pair of elements acting in transmission and reception. This collection of A-scans, of which there will be N^2 for an array with N elements, is referred to as the full matrix of data for an array. Holmes et al introduced the total focusing method (TFM), which utilizes the full matrix data, and showed that it outperforms standard imaging methods such as planar B-scans, sector B-scans (called S-scans), and focused B-scans [9]. Many variations of the total focusing method have been developed including, but not limited to,

- Corrected TFM, which attempts to remove the effects of beam spread, attenuation, and directivity [10]. Similarly, Levesque et al improved the performance of the TFM by Wiener deconvolution with a reference signal, limiting the bandwidth on which the calculations are performed to that of the system, and by finding the optimal aperture [11].
- Vector TFM (VTFM), which shows an approximate orientation of the reflector being imaged [12].
- Diffraction TFM, which is the application of TFM to TOFD-type inspections [12].
- Common source method (CSM) and the synthetic aperture focusing technique (SAFT), which are special cases of TFM since they use subsets of the full matrix data [13].

www.manaraa.com

Velichko and Wilcox provide a theoretical comparison of the TFM to other linear full matrix imaging methods [14], and Zhang et al compare the TFM to nonlinear full matrix methods for the case of noisy data [15]. Wilcox provides an excellent overview of the current state of phased array imaging [16].

Imaging methods such as TFM, CSM, and SAFT are all examples of what can be called data-driven imaging methods since they form images directly from the measured A-scan voltage signals. Thus, they do not provide images that can be directly related to flaw properties. In Chapter 3 a new imaging method will be presented that is closely related to the TFM, CSM, and SAFT approaches but does define the image generated in terms of specific flaw characteristics.

Physical optics far-field inverse scattering

In 1967 Bojarski introduced the physical optics far-field inverse scattering (POFFIS) method, which relates the three-dimensional characteristic function of a scatterer to the spatial Fourier transform of its far-field normalized scattering amplitude [4]. However, in real band-limited and aperture-limited measurements, obtaining a meaningful image of a characteristic function is problematic. Bleistein first tried to overcome that limitation of POFFIS by calculating the derivative of the characteristic function rather than the characteristic function itself [17], and later Cohen and Bleistein introduced the singularity function of the flaw surface, which is the normal derivative of the characteristic function, to turn POFFIS into a practical imaging method [18]. In Chapter 3 it will be shown that the new imaging method is a generalization of POFFIS that, for small flaws, provides explicit images of the surface reflectivity of the flaw.

Thesis Organization

This thesis is written in a format where the next two chapters each contain a journal paper. Chapter 2 will show how phased arrays can implement equivalent flaw sizing of cracks (and

www.manaraa.com

potentially other flaws) in a simple and cost-effective manner. It is a paper to be submitted to *NDT&E International*. Chapter 3 will show the development of a new quantitative imaging algorithm and demonstrate its performance with simulations. This paper will be submitted to *Ultrasonics*. A set of overall conclusions and recommendations for future work is given in Chapter 4.

www.manaraa.com

CHAPTER 2. EQUIVALENT FLAW TIME-OF-FLIGHT DIFFRACTION SIZING WITH ULTRASONIC PHASED ARRAYS

Brady J. Engle[1,2], Lester W. Schmerr, Jr.[1,2], Alexander Sedov[3]

[1]Center for Nondestructive Evaluation, Iowa State University, Ames, IA 50011

[2]Department of Aerospace Engineering, Iowa State University, Ames, IA 50011

[3]Department of Mechanical Engineering, Lakehead University, Thunder Bay, ON, Canada

A paper originally published in the proceedings of the annual *Review of Progress in Quantitative Nondestructive Evaluation* [19].

Abstract

Ultrasonic phased array transducers can be used to extend traditional time-of-flight diffraction (TOFD) crack sizing, resulting in more quantitative information about the crack being obtained. Traditional TOFD yields a single length parameter, while the equivalent flaw time-of-flight diffraction crack sizing method (EFTOFD) described here uses data from multiple look-angles to fit an equivalent degenerate ellipsoid to the crack. The size and orientation of the equivalent flaw can be used to estimate the actual crack size. The method is presented with experimental validation for isolated cracks, and a brief overview of extending the method to surface-breaking cracks and volumetric flaws is given.

www.manaraa.com

Introduction

Time-of-flight diffraction sizing (TOFD) was developed in the 1970s and is widely used to estimate crack lengths in welds. TOFD uses the time difference, Δt, between scattered diffraction signals from the crack tips to estimate the length of the crack. Traditionally, the TOFD method is done in a pitch-catch arrangement using single-element transducers. No detailed flaw geometry or orientation information is obtained through TOFD sizing, only a single length parameter [3].

A separate time-of-flight-based crack sizing method developed in the 1980s and 1990s used a multi-viewing transducer system, which was composed of multiple conventional transducers arranged conically, to inspect flaws from multiple incident wave directions, or look-angles [7]. A sizing algorithm used the Δt data from different look-angles to estimate the crack size as a best-fit degenerate ellipsoid [8].

This work uses phased array transducers to extend traditional TOFD by incorporating the equivalent flaw sizing algorithm developed with the multi-viewing transducer system. This allows for a single array transducer in pulse-echo or a pair of array transducers in pitch-catch to estimate the size and orientation of a crack in what we will call the equivalent flaw time-of-flight diffraction sizing method, or EFTOFD. The EFTOFD method can be done in nearly the same amount of time as traditional TOFD by making a few more measurements and processing the data with a computationally inexpensive sizing algorithm. The algorithm will be developed and experimentally validated for isolated cracks, then an extension of the method to surface-breaking cracks and volumetric flaws will be presented.

Crack Sizing Algorithm

Figure 2.1 depicts an immersion, pulse-echo interrogation of a horizontal elliptical crack with a phased array transducer. A coordinate system fixed with respect to the sample with axes x, y, and z can be arbitrarily chosen, and the equivalent flaw size and orientation will

www.manaraa.com

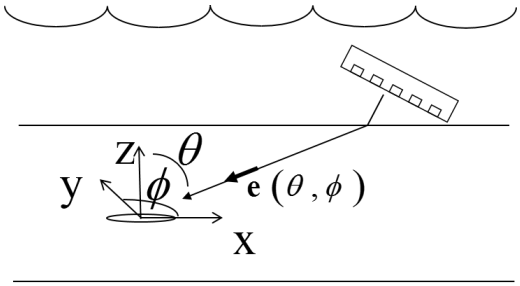

Figure 2.1: Pulse-echo immersion setup for EFTOFD sizing of an isolated horizontal crack.

be expressed in this coordinate system. The angles ϕ and θ, shown in Fig. 2.1, define the incident wave direction $\mathbf{e}(\theta, \phi)$. The angle θ is a rotation in a plane containing the z-axis, and the angle ϕ is a rotation about the z-axis. To obtain an angle ϕ, the sample can be rotated about the z-axis, or the incident beam can be mechanically rotated or electronically steered the same amount in the opposite direction. The angle θ can be changed either by mechanically rotating the transducer or electronically steering the beam. Incident waves from the transducer, with direction given by $\mathbf{e}$, will result in a specularly scattered wave from the crack surface, two diffracted signals from the crack edges, and other, usually smaller, crack responses. If the angle θ is such that the specularly reflected wave does not return to the transducer, the diffracted signals will be seen primarily. Figure 2.2 shows a simulated A-scan with well-separated crack edge diffraction signals. The time difference, Δt, is defined as the time between peaks of these crack edge signals. Obtaining a small number of these Δt measurements from different

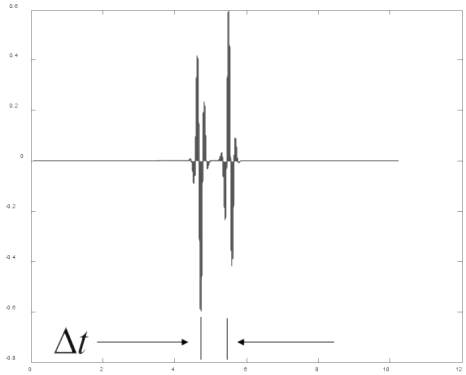

Figure 2.2: Simulated crack edge diffraction signals and the associated Δt.

www.manaraa.com

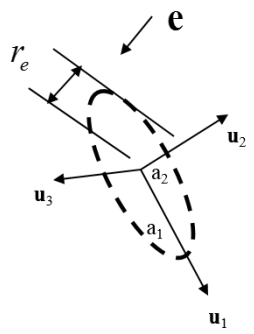

Figure 2.3: Equivalent radius r_e for incident wave direction **e**.

incident vectors **e** and solving a linear least squares and eigenvalue problem will allow the determination of an equivalent ellipse [8].

Schmerr has shown [2] that the Δt data for each look-angle, **e**, is related to the equivalent radius, r_e, of an elliptical shaped crack in the direction of **e** given by

$$r_e = c\Delta t/4 \tag{2.1}$$

where the equivalent radius is the distance between the center of the ellipse and its edge in the **e** direction (see Fig. 2.3). Figure 2.3 shows the incident vector **e** and equivalent radius r_e, along with the semi-major and -minor axes a_1 and a_2 of the ellipse and their directions $\mathbf{u}_1$ and $\mathbf{u}_2$. The direction $\mathbf{u}_3$ corresponds to the crack surface normal. Expressing the equivalent radius in terms of the incident wave direction **e** and the ellipsoid parameters a_1, a_2, a_3 and $\mathbf{u}_1$, $\mathbf{u}_2$, $\mathbf{u}_3$ gives [2]

$$r_e^2 = a_1^2(\mathbf{e}\cdot\mathbf{u}_1)^2 + a_2^2(\mathbf{e}\cdot\mathbf{u}_2)^2 + a_3^2(\mathbf{e}\cdot\mathbf{u}_3)^2. \tag{2.2}$$

Equation 2.2 can be rewritten as

$$r_e^2(\mathbf{C},\mathbf{e}) = C_{xx}e_x^2 + C_{yy}e_y^2 + C_{zz}e_z^2 + C_{xy}e_xe_y + C_{xz}e_xe_z + C_{yz}e_ye_z \tag{2.3}$$

where

$$\begin{aligned}
C_{xx} &= a_1^2u_{1x}^2 + a_2^2u_{2x}^2 + a_3^2u_{3x}^2 & C_{xy} &= 2(a_1^2u_{1x}u_{1y} + a_2^2u_{2x}u_{2y} + a_3^2u_{3x}u_{3y}) \\
C_{yy} &= a_1^2u_{1y}^2 + a_2^2u_{2y}^2 + a_3^2u_{3y}^2 & C_{xz} &= 2(a_1^2u_{1x}u_{1z} + a_2^2u_{2x}u_{2z} + a_3^2u_{3x}u_{3z}) \\
C_{zz} &= a_1^2u_{1z}^2 + a_2^2u_{2z}^2 + a_3^2u_{3z}^2 & C_{yz} &= 2(a_1^2u_{1y}u_{1z} + a_2^2u_{2y}u_{2z} + a_3^2u_{3y}u_{3z}).
\end{aligned} \tag{2.4}$$

www.manaraa.com

Using Eqs. 2.1 and 2.3 we can define a function, F_m, and error function for M measurements where Δt_m and $\mathbf{e}_m$ are the m^{th} time difference and incident wave direction, respectively.

$$F_m = \left(\frac{c\Delta t_m}{4}\right)^2 - r_e^2(\mathbf{C}, \mathbf{e}_m) \tag{2.5}$$

$$E(\mathbf{C}) = \sum_{m=1}^{M} F_m^2 \tag{2.6}$$

Minimizing the error function, i.e.

$$\frac{\partial E}{\partial C_{ij}} = 0 \qquad (i, j = 1,2,3), \tag{2.7}$$

yields a system of linear equations for the $\mathbf{C}$ parameters, which can then be used to solve the eigenvalue problem

$$\sum_{j=1}^{3} (C_{ij} - \lambda \delta_{ij}) l_j \qquad (i = 1,2,3). \tag{2.8}$$

It can be shown [2] that the eigenvalues of $\mathbf{C}$ are just the lengths of the semi-major axes of the equivalent ellipsoid and the eigenvectors are the corresponding directions:

$$\lambda = \begin{pmatrix} a_1^2 \\ a_2^2 \\ a_3^2 \end{pmatrix} \qquad \mathbf{l} = \begin{pmatrix} \mathbf{u}_1 & \mathbf{u}_2 & \mathbf{u}_3 \end{pmatrix}. \tag{2.9}$$

Model-Based Bandwidth Error Correction

The Δt measurements are subject to errors due to the finite bandwidth of the ultrasonic system. These errors can be corrected by using modeling to generate an error correction curve [8], as shown in Fig. 2.4. The ideal, infinite bandwidth crack edge diffraction signals are modeled using the scattering amplitude given by the Kirchhoff approximation [2]. The exact Δt values, shown as Δt_e in Fig. 2.4, are taken to be the time differences between these modeled signals. Convolving the Kirchhoff scattering amplitude with a Gaussian distribution, which represents the limited bandwidth of the system, results in a band-limited representation of the diffraction signals. The time differences between peaks of these limited bandwidth signals are

www.manaraa.com

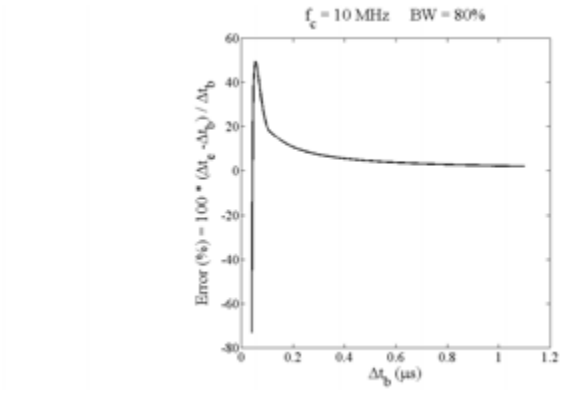

Figure 2.4: Model-based bandwidth error correction curve.

taken to be the band-limited Δt values, shown as Δt_b in Fig. 2.4. For larger cracks the bandwidth corrections are positive, but as the crack becomes smaller, the bandwidth rather than the crack size controls the measured Δt and the errors rapidly become negative. The transition between these positive and negative errors defines the smallest possible Δt values that can be used for a given bandwidth.

Experimental Results

The experimental setup used is depicted in Fig. 2.1. Two flaws were examined: the first was a #5 flat bottom hole (FBH) with a 1.984 mm diameter in 7075-T651 aluminum, and the second was an elliptical shaped isolated crack-like flaw that was manufactured in a diffusion-bonded titanium sample [20, 21]. The elliptical crack was designed to have a semi-major axis of 2.5 mm and a semi-minor axis of 0.6 mm. These flaws are suitable for simulating crack responses because they both exhibit strong edge diffraction signals. The flaws were oriented during the inspection such that the crack surface normal $\mathbf{u}_3$ was in the z-direction, and the elliptical flaw had the semi-major and -minor axes $\mathbf{u}_1$ and $\mathbf{u}_2$ in the x- and y-directions, respectively.

A 32 element, 10 MHz linear array transducer with a 0.31 mm pitch was used to carry out the inspection. Time delay laws were employed to change the angle θ electronically, while the samples were rotated to change the angle ϕ. Note that the use of a 2-D array would allow both

www.manaraa.com

Table 2.1: Data table for 1.984 mm diameter FBH.

θ (deg)	ϕ (deg)	Meas. Δt (μs)	Meas. Δt (μs) with BW Corr.	Exact Δt (μs)
75	00	0.55	0.57	0.609
75	30	0.54	0.56	0.609
75	60	0.54	0.56	0.609
70	00	0.52	0.54	0.592
70	30	0.53	0.55	0.592
70	60	0.54	0.56	0.592
65	00	0.52	0.54	0.571
65	30	0.51	0.53	0.571
65	60	0.50	0.52	0.571
60	00	0.50	0.52	0.546
60	30	0.49	0.51	0.546
60	60	0.48	0.50	0.546

angles to be changed electronically. Twelve look-angles were used for each flaw, and the Δt data can be seen in Table 2.1 for the FBH and Table 2.2 for the elliptical crack.

Table 2.2: Data table for 5x1.2 mm (major x minor axes) elliptical crack.

θ (deg)	ϕ (deg)	Meas. Δt (μs)	Meas. Δt (μs) with BW Corr.	Exact Δt (μs)
55	90	0.33	0.35	0.318
55	60	0.69	0.71	0.718
55	45	0.93	0.95	0.964
50	90	0.33	0.35	0.298
50	60	0.65	0.67	0.671
50	45	0.85	0.87	0.901
45	90	0.31	0.33	0.275
45	60	0.56	0.58	0.620
45	45	0.78	0.80	0.832
40	90	0.26	0.28	0.250
40	60	0.53	0.55	0.563
40	45	0.69	0.71	0.756

The tables show the θ and ϕ values along with the measured Δt values in μs, the bandwidth-corrected measured Δt values, and the exact Δt values obtained through Eq. 2.2. Cracks with irregular shapes may require additional look-angles over a wider range of angles to estimate the size accurately.

www.manaraa.com

Equation 2.10 shows the exact results for the FBH, Eq. 2.11 shows the EFTOFD results with no bandwidth correction, and Eq. 2.12 shows the EFTOFD results with the bandwidth correction.

$$\begin{pmatrix} a_1 \\ a_2 \\ a_3 \end{pmatrix} = \begin{pmatrix} 0.992 \\ 0.992 \\ 0 \end{pmatrix} \qquad \begin{pmatrix} u_{1x} & u_{2x} & u_{3x} \\ u_{1y} & u_{2y} & u_{3y} \\ u_{1z} & u_{2z} & u_{3z} \end{pmatrix} = \begin{pmatrix} \cdot & \cdot & 0 \\ \cdot & \cdot & 0 \\ 0 & 0 & 1 \end{pmatrix} \tag{2.10}$$

$$\begin{pmatrix} a_1 \\ a_2 \\ a_3 \end{pmatrix} = \begin{pmatrix} 0.9 \\ 0.9 \\ 0.3i \end{pmatrix} \qquad \begin{pmatrix} u_{1x} & u_{2x} & u_{3x} \\ u_{1y} & u_{2y} & u_{3y} \\ u_{1z} & u_{2z} & u_{3z} \end{pmatrix} = \begin{pmatrix} 0.2 & -1.0 & -0.2 \\ -1.0 & -0.2 & 0.2 \\ 0.2 & -0.1 & 1.0 \end{pmatrix} \tag{2.11}$$

$$\begin{pmatrix} a_1 \\ a_2 \\ a_3 \end{pmatrix} = \begin{pmatrix} 1.0 \\ 0.9 \\ 0.2i \end{pmatrix} \qquad \begin{pmatrix} u_{1x} & u_{2x} & u_{3x} \\ u_{1y} & u_{2y} & u_{3y} \\ u_{1z} & u_{2z} & u_{3z} \end{pmatrix} = \begin{pmatrix} 0.2 & -1.0 & -0.2 \\ -1.0 & -0.2 & 0.2 \\ 0.2 & -0.1 & 1.0 \end{pmatrix} \tag{2.12}$$

The dots in Eq. 2.10 are present because the FBH is circular, and the major and minor axes can be any set of perpendicular directions in the *x*-*y* plane.

Equation 2.13 shows the exact results for the elliptical crack, and Eqs. 2.14 and 2.15 show the EFTOFD results without and with the bandwidth correction, respectively.

$$\begin{pmatrix} a_1 \\ a_2 \\ a_3 \end{pmatrix} = \begin{pmatrix} 2.5 \\ 0.6 \\ 0 \end{pmatrix} \qquad \begin{pmatrix} u_{1x} & u_{2x} & u_{3x} \\ u_{1y} & u_{2y} & u_{3y} \\ u_{1z} & u_{2z} & u_{3z} \end{pmatrix} = \begin{pmatrix} 1 & 0 & 0 \\ 0 & 1 & 0 \\ 0 & 0 & 1 \end{pmatrix} \tag{2.13}$$

$$\begin{pmatrix} a_1 \\ a_2 \\ a_3 \end{pmatrix} = \begin{pmatrix} 2.5 \\ 0.7 \\ 0.7i \end{pmatrix} \qquad \begin{pmatrix} u_{1x} & u_{2x} & u_{3x} \\ u_{1y} & u_{2y} & u_{3y} \\ u_{1z} & u_{2z} & u_{3z} \end{pmatrix} = \begin{pmatrix} -1.0 & 0.0 & 0.1 \\ 0.0 & 0.9 & -0.5 \\ 0.1 & 0.5 & 0.9 \end{pmatrix} \tag{2.14}$$

$$\begin{pmatrix} a_1 \\ a_2 \\ a_3 \end{pmatrix} = \begin{pmatrix} 2.5 \\ 0.7 \\ 0.7i \end{pmatrix} \qquad \begin{pmatrix} u_{1x} & u_{2x} & u_{3x} \\ u_{1y} & u_{2y} & u_{3y} \\ u_{1z} & u_{2z} & u_{3z} \end{pmatrix} = \begin{pmatrix} -1.0 & 0.0 & 0.1 \\ 0.0 & 0.9 & -0.5 \\ 0.1 & 0.5 & 0.9 \end{pmatrix} \tag{2.15}$$

www.manaraa.com

The a_3 values in Eqs. 2.11, 2.12, 2.14, and 2.15 are imaginary because the a_3^2 values returned by the eigenvalue problem are small, often negative numbers. Taking the square root of a negative value of a_3^2 results in an imaginary a_3. The a_1 and a_2 values for both flaws are estimated to within 20% of their actual values, and the orientation results show good agreement with the expected values. The crack surface normal $\mathbf{u}_3$ for both flaws is estimated as primarily in the z-direction, as expected. Equations 2.14 and 2.15 show that for the elliptical crack the semi-major and -minor axes $\mathbf{u}_1$ and $\mathbf{u}_2$ are predominately along the x- and y-directions, respectively, which was also expected.

The sizing results for these flaws only differ slightly when the bandwidth correction is applied. This is due to most of the Δt values being large enough that the errors are relatively small. Figure 2.4 shows that the errors for many of the Δt values encountered are only a few percent. The bandwidth correction becomes more important for smaller flaws, whose smaller Δt values would have much larger errors. However, Table 2.1 shows that, for the FBH, the Δt values with the bandwidth correction are all closer to the exact values than the Δt values without the correction, showing that the bandwidth correction is removing some systematic error. Table 2.2 shows that 8 of the 12 Δt measurements are closer to the exact values with the bandwidth correction than without for the elliptical crack. It is worth noting that all four measurements that did not get closer to the exact values were made with $\phi = 90^\circ$, which corresponds to the shortest length across the crack surface. These may be due to small errors in the assumed orientation of the ellipse.

Extension to Other Flaws

In addition to isolated cracks, an equivalent flaw sizing approach can potentially be applied to surface-breaking cracks and volumetric flaws such as voids and inclusions. These setups can be seen in Figs. 2.5a and 2.5b. Unlike the isolated crack case which has two diffraction signals, the surface-breaking crack only has one. Volumetric flaws will produce no significant

www.manaraa.com

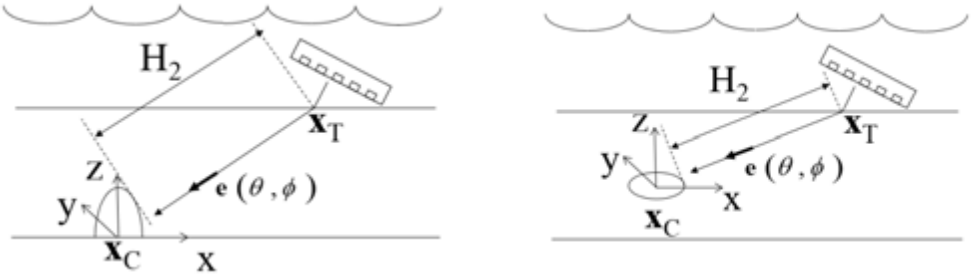

(a) Pulse-echo immersion setup for the EFTOFD sizing of a surface-breaking crack.

(b) Pulse-echo immersion setup for the EFTOFD sizing of a volumetric flaw.

Figure 2.5: Pulse-echo immersion setup for the EFTOFD sizing of (a) surface-breaking crack and (b) volumetric flaw.

edge diffraction signals, so the method technically cannot be called EFTOFD for this case but it is included here because of the applicability of the approach to these flaws. The primary difference in the algorithms for these cases and the isolated crack case is that the surface-breaking and volumetric algorithms need absolute time-of-flight information in order to solve for both the location of the flaw center and the equivalent size and orientation parameters of the flaw [22]. To accurately estimate the size and location of volumetric flaws, at least one look-angle should involve the far side of the flaw through a reflection off of the back surface of the sample [22]. For surface-breaking cracks, the corner trap signal, which is the wave specularly reflected from the back surface of the part and then from the crack surface, may be used in a similar way.

Applying this method to the geometries in Figs. 2.5a and 2.5b can be done by defining a function F_m as [22]

$$F_m = (\mathbf{x}_{Tm}\cdot\mathbf{e}_m - H_{2m})^2 - 2(\mathbf{x}_{Tm}\cdot\mathbf{e}_m - H_{2m})(\mathbf{x}_C\cdot\mathbf{e}_m) + (\mathbf{x}_C\cdot\mathbf{e}_m)^2 - C_{ij}e_{im}e_{jm} \tag{2.16}$$

and an error function again as

$$E(\mathbf{C}) = \sum_{m=1}^{M} F_m^2. \tag{2.17}$$

Minimizing this error function, i.e.

$$\frac{\partial E}{\partial x_{Cj}} = 0 \qquad (j = 1,2,3), \tag{2.18}$$

www.manaraa.com

$$\frac{\partial E}{\partial C_{ij}} = 0 \qquad (i,j = 1,2,3), \tag{2.19}$$

results in a nonlinear set of equations that can be solved for $\mathbf{x}_C$ and $\mathbf{C}$. The nonlinearity is quadratic, so solving the equations is a relatively straightforward process. After solving for $\mathbf{x}_C$ and $\mathbf{C}$, the eigenvalue problem can be solved in the same way as discussed previously. Schmerr et al have done a preliminary numerical analysis of the surface-breaking crack case which has shown promising results [23].

Conclusion

The equivalent flaw time-of-flight diffraction (EFTOFD) sizing method has been shown to accurately determine the size and orientation of isolated crack-like flaws using a linear phased array. Adaption of this method to phased arrays makes it a practical sizing tool with standard phased array instrumentation. The use of a linear array required some mechanical motion of the array (or the part) to acquire the data but the replacement with a 2-D array can potentially eliminate or reduce this requirement. Using a relatively small number of measurements with a computationally inexpensive processing algorithm allows the EFTOFD method to obtain quantitative flaw size and orientation information in contrast to traditional TOFD sizing which obtains only a length parameter of a crack in an a priori assumed orientation. This additional information is important in fracture mechanics studies to determine the significance of the crack from a safety and reliability standpoint.

www.manaraa.com

CHAPTER 3. QUANTITATIVE IMAGING WITH ULTRASONIC PHASED ARRAYS

Brady J. Engle[1,2], Lester W. Schmerr, Jr.[1,2], Alexander Sedov[3]

[1]Center for Nondestructive Evaluation, Iowa State University, Ames, IA 50011

[2]Department of Aerospace Engineering, Iowa State University, Ames, IA 50011

[3]Department of Mechanical Engineering, Lakehead University, Thunder Bay, ON, Canada

Abstract

Ultrasonic imaging is a crucial tool not only for NDE applications, but for use in the medical industry as well. Having confidence in the images is essential in both fields, but often the flaws present in NDE inspections are small enough to be near the resolution limit of the system. This affects how reliably the image can be used to directly evaluate small flaws. Ultrasonic phased array transducers, which have the ability to obtain data from all combinations of elements acting in transmission and reception, allow for the formation of advanced images beyond what is possible with traditional single-element transducers. Often the images formed are based on ad-hoc imaging methods which makes them largely qualitative in nature. The goal of this work is to present a model-based imaging algorithm that results in images being formed that are quantitatively indicative of actual flaw properties and to use this algorithm to evaluate and understand the image formation process.

www.manaraa.com

Introduction

Phased array transducers are a valuable tool for ultrasonic imaging. However, in many practical applications, image formation methods are used (B-scans, C-scans, S-scans, etc.) that are similar to those developed for single-element transducers. Such methods are ad-hoc methods that do not take advantage of the unique capabilities of arrays.

Arrays can also be used to make images in more advanced ways than possible with single-element transducers. Techniques such as the total focusing method (TFM) [9] and the synthetic aperture focusing technique (SAFT) [13] utilize an array's ability to capture signals from every combination of elements acting in transmission and reception to form images that are essentially focused everywhere in a spatial grid of image points. SAFT and TFM are still, however, ad-hoc methods where there is no meaning attached to the values in the image, which makes flaw characterization difficult especially for small flaws. To quantitatively characterize small flaws using imaging, the image formation process needs to be more closely examined.

The goal of this work is to develop and use a model-based approach to understand how the received voltages are a function of both the ultrasonic system and the flaw present so that images can be formed that are explicit functions of only the flaw properties. First, an overview of the SAFT and TFM methods will be given with experimental examples. Then we will develop new model-based quantitative imaging algorithms that will explicitly connect the image being formed with the properties of the flaw. Finally, we will use these new models to form images with simulated data and study the quantitative nature of those images.

Synthetic aperture focusing technique (SAFT)

SAFT, while commonly used today with phased arrays, was originally performed by moving a single-element transducer along a line. For phased arrays, a SAFT image can be formed by first defining a 2-D grid of points to be imaged and calculating the travel time for a wave propagating from the centroid of each array element to each grid point. Then, for each image

www.manaraa.com

point, the pulse-echo voltage signals from each element are advanced by twice the travel time – the time from the element centroid to the image point and back to the centroid – and these advanced signals are summed. The value of this sum at time $t = 0$ is taken to be the amplitude of the image at that image point. For a linear array with N elements, the travel time between the centroid of the n^{th} element, $\mathbf{X}_{cn}$, and the current image point $\mathbf{Y}$, is denoted by $T(\mathbf{X}_{cn}, \mathbf{Y})$. With the voltages given by $V(\mathbf{X}_{cn}, t)$, the image value at point $\mathbf{Y}$ can be calculated as

$$I_{SAFT}(\mathbf{Y}) = \sum_{n=1}^{N} V(\mathbf{X}_{cn}, t + 2T(\mathbf{X}_{cn}, \mathbf{Y}))\Big|_{t=0}. \tag{3.1}$$

Noting that the voltages can be written in terms of their Fourier transforms as

$$V(\mathbf{X}_{cn}, t) = \frac{1}{2\pi} \int_{-\infty}^{+\infty} V(\mathbf{X}_{cn}, \omega) \exp(-i\omega t) d\omega \tag{3.2}$$

a Fourier transform version of SAFT can be shown to be

$$\begin{aligned} I_{SAFT}(\mathbf{Y}) &= \sum_{n=1}^{N} \frac{1}{2\pi} \int_{-\infty}^{+\infty} V(\mathbf{X}_{cn}, \omega) \exp(-i\omega(t + 2T(\mathbf{X}_{cn}, \mathbf{Y}))) d\omega \Big|_{t=0} \\ &= 2 \text{ Re} \left(\sum_{n=1}^{N} \frac{1}{2\pi} \int_{0}^{+\infty} V(\mathbf{X}_{cn}, \omega) \exp(-2i\omega T(\mathbf{X}_{cn}, \mathbf{Y})) d\omega \right) \end{aligned} \tag{3.3}$$

which, when the frequency integration is discretized, is

$$I_{SAFT}(\mathbf{Y}) = 2 \text{ Re} \left(\frac{\Delta\omega}{2\pi} \sum_{m=1}^{M} \sum_{n=1}^{N} V(\mathbf{X}_{cn}, \omega_m) \exp(-2i\omega_m T(\mathbf{X}_{cn}, \mathbf{Y})) \right). \tag{3.4}$$

Total focusing method (TFM)

The main difference between SAFT and TFM is that TFM uses the voltage signals from all element pairs instead of only the pulse-echo signals, as SAFT does. This means that the time advance present in the TFM equation will be the sum of the travel time from the centroid of the transmitting element to the image point, $T(\mathbf{X}_s, \mathbf{Y})$, and the travel time from the image point to the centroid of the receiving element, $T(\mathbf{X}_r, \mathbf{Y})$. The time domain TFM for a linear array with N elements is given by

www.manaraa.com

$$I_{TFM}(\mathbf{Y}) = \sum_{n=1}^{N}\sum_{l=1}^{N} V(\mathbf{X}_{sn}, \mathbf{X}_{rl}, t + T(\mathbf{X}_{sn}, \mathbf{Y}) + T(\mathbf{X}_{rl}, \mathbf{Y}))\Big|_{t=0} \tag{3.5}$$

and, similar to the SAFT case, the discretized frequency domain TFM is

$$I_{TFM}(\mathbf{Y}) = 2\,\mathrm{Re}\left(\frac{\Delta\omega}{2\pi}\sum_{m=1}^{M}\sum_{n=1}^{N}\sum_{l=1}^{N} V(\mathbf{X}_{sn}, \mathbf{X}_{rl}, \omega_m)\exp(-i\omega_m T(\mathbf{X}_{sn}, \mathbf{Y}) - i\omega_m T(\mathbf{X}_{rl}, \mathbf{Y}))\right). \tag{3.6}$$

SAFT/TFM discussion

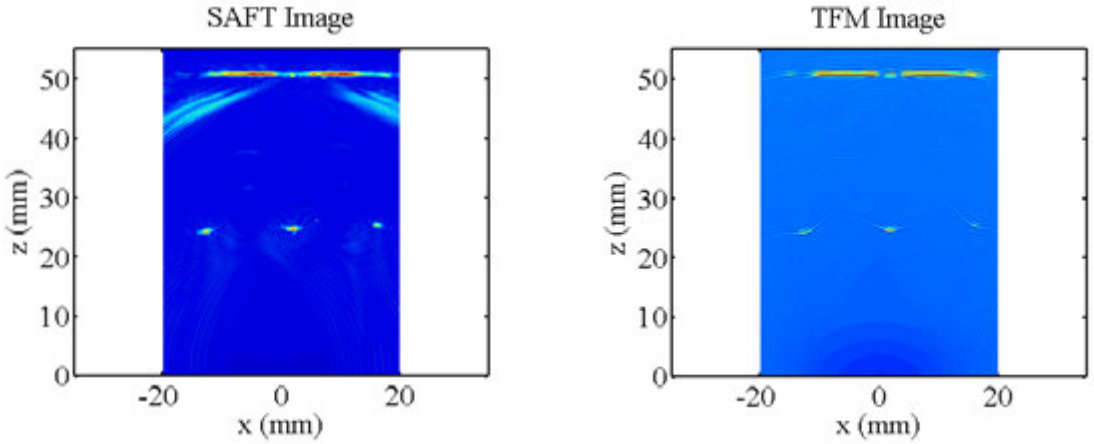

(a) SAFT Image. (b) TFM Image.

Figure 3.1: SAFT and TFM images for a 2 inch thick aluminum sample with side-drilled holes of 2, 3, and 4 millimeter diameters.

Figure 3.1a shows a SAFT image of a two inch thick aluminum block with side-drilled holes of 2, 3, and 4 millimeters, and Fig. 3.1b shows a TFM image of the same sample. The array was placed directly on the block and is centered at $(x(mm), z(mm)) = (0,0)$. The front surface of the block is along the line $z(mm) = 0$, and the back surface is along $z(mm) = 50.8$. The time advances – twice the travel time from the element centroid to the image point for SAFT and the sum of the travel time from the sending element centroid to the image point and from the image point to the receiving element centroid for TFM – are essentially using post-processing to focus the beam in transmission and reception at every image point. If a reflector is present at an image point the summation of signals should result in a large value, while if no

www.manaraa.com

reflector is present, the summation should produce a small value. The responses of the three side-drilled holes as well as the back surface of the sample can be seen in both the SAFT and TFM images in Fig. 3.1, but little quantitative information can be obtained from these images.

Quantitative Imaging Algorithm

To develop a more quantitative imaging method, we will consider a 2-D problem where 1-D array elements are radiating directly into a fluid. This 2-D case will allow us to examine the imaging process in detail in a computationally efficient manner while still retaining much of the important physics of the image formation process. For small flaws the measured voltage received at an element with centroid location $\mathbf{X}_r$ from a small flaw whose center is at $\mathbf{X}_0$ and is being insonified by a transmitting element with centroid at $\mathbf{X}_s$ can be expressed in the scalar 2-D form of the Thompson-Gray measurement model [24, 2]

$$\begin{aligned} V(\mathbf{X}_s,\mathbf{X}_r,\omega) =& s_I(\omega)\hat{P}^{(1)}(\mathbf{X}_s,\mathbf{X}_0,\omega)\hat{P}^{(2)}(\mathbf{X}_r,\mathbf{X}_0,\omega)A(\mathbf{e}_{inc};\mathbf{e}_{scat}) \\ &\cdot\left[\frac{1}{-ik_2 l_A}\frac{\rho c}{\rho_2 c_2}\sqrt{-8\pi i k_2}\right] \end{aligned} \tag{3.7}$$

where

$$A(\mathbf{e}_{inc};\mathbf{e}_{scat}) = -\sqrt{\frac{i}{8\pi k_2}}\int_{C_f}\left[\frac{\partial\overline{p}^{(1)}}{\partial n}+ik_2(\mathbf{e}_{scat}\cdot\mathbf{n})\overline{p}^{(1)}\right]\exp\left[-ik_2\mathbf{e}_{scat}\cdot(\mathbf{X}-\mathbf{X}_0)\right]ds(\mathbf{X}) \tag{3.8}$$

is the far-field scattering amplitude, and

$$\overline{p}^{(1)} = \frac{p^{(1)}}{P^{(1)}(\mathbf{X}_s,\mathbf{X}_0,\omega)\exp[i\omega T(\mathbf{X}_s,\mathbf{X}_0)]}, \tag{3.9}$$

is the normalized pressure field. The superscripts (1) and (2) correspond to two separate states. State (1) is the actual inspection setup: transmitting element acting in transmission, receiving element acting in reception, and the flaw is present. State (2) corresponds to the receiving element acting in transmission, the transmitting element acting in reception, and the flaw is absent. The quantity l_A is the length of an array element. The quantities ρ_1, c_1, and k_1 are the

www.manaraa.com

density, wavespeed, and wavenumber for the material surrounding the transmitting transducer, ρ_2, c_2, and k_2 correspond to those properties for the material around the flaw, and ρ, c, and k are these same properties at the receiving transducer. ρ_3, c_3, and k_3 correspond to the material properties within the flaw. Note that for an array radiating into a single medium, all of these properties are identical. In Eq. 3.7 the $\hat{P}^{(1)}(\mathbf{X}_s,\mathbf{X}_0,\omega)$ and $\hat{P}^{(2)}(\mathbf{X}_r,\mathbf{X}_0,\omega)$ terms are non-dimensional pressure amplitudes of the incident waves at $\mathbf{X}_0$ in states (1) and (2)

$$\hat{P}^{(1)}(\mathbf{X}_s,\mathbf{X}_0,\omega) = \frac{P^{(1)}(\mathbf{X}_s,\mathbf{X}_0,\omega)}{\rho_1 c_1 v_T^{(1)}} \exp[i\omega T(\mathbf{X}_s,\mathbf{X}_0)] \tag{3.10}$$

$$\hat{P}^{(2)}(\mathbf{X}_r,\mathbf{X}_0,\omega) = \frac{P^{(2)}(\mathbf{X}_r,\mathbf{X}_0,\omega)}{\rho c v_R^{(2)}} \exp[i\omega T(\mathbf{X}_r,\mathbf{X}_0)]. \tag{3.11}$$

These incident waves can be calculated with ultrasonic beam models. The $s_I(\omega)$ term in Eq. 3.7 is called the system function, and it depends on the electrical and electromechanical parts of the ultrasonic system [25].

To calculate the flaw scattering amplitude one needs to know the total wave field (incident and scattered waves) in state (1). This pressure field can be obtained explicitly with the Kirchhoff approximation as [2]

$$\begin{aligned}
p^{(1)} &= P^{(1)}(\mathbf{X}_s,\mathbf{X},\omega)\exp\left[i\omega T(\mathbf{X}_s,\mathbf{X})\right](1+R_{23}) \\
&= P^{(1)}(\mathbf{X}_s,\mathbf{X}_0,\omega)\exp\left[i\omega T(\mathbf{X}_s,\mathbf{X})\right]\exp\left[i\omega \mathbf{e}^{(1)}\cdot(\mathbf{X}-\mathbf{X}_0)/c_2\right](1+R_{23}) \\
\frac{\partial p^{(1)}}{\partial n} &= ik_2 P^{(1)}(\mathbf{X}_s,\mathbf{X},\omega)\exp\left[i\omega T(\mathbf{X}_r,\mathbf{X})\right]\left((\mathbf{e}_{inc}\cdot\mathbf{n})+R_{23}(\mathbf{e}_r\cdot\mathbf{n})\right) \\
&= ik_2 P^{(1)}(\mathbf{X}_s,\mathbf{X}_0,\omega)\exp\left[i\omega T(\mathbf{X}_r,\mathbf{X}_0)\right]\exp\left[i\omega \mathbf{e}^{(1)}\cdot(\mathbf{X}-\mathbf{X}_0)/c_2\right] \\
&\quad\cdot\left((\mathbf{e}_{inc}\cdot\mathbf{n})+R_{23}(\mathbf{e}_r\cdot\mathbf{n})\right)
\end{aligned} \tag{3.12}$$

which implies

$$\begin{aligned}
\overline{p}^{(1)} &= \exp\left[i\omega \mathbf{e}^{(1)}\cdot(\mathbf{X}-\mathbf{X}_0)/c_2\right](1+R_{23}) \\
\frac{\partial \overline{p}^{(1)}}{\partial n} &= ik_2\exp\left[i\omega \mathbf{e}^{(1)}\cdot(\mathbf{X}-\mathbf{X}_0)/c_2\right]\left((\mathbf{e}_{inc}\cdot\mathbf{n})+R_{23}(\mathbf{e}_r\cdot\mathbf{n})\right).
\end{aligned} \tag{3.13}$$

www.manaraa.com

Here R_{23} is the plane wave reflection coefficient for the interface of the flaw material and the material surrounding the flaw, given as

$$R_{23} = \frac{Z_3 - Z_2}{Z_3 + Z_2} = \frac{\rho_3 c_3 - \rho_2 c_2}{\rho_3 c_3 + \rho_2 c_2} \tag{3.14}$$

where Z denotes the acoustic impedance for a material. Also, $\mathbf{e}^{(1)} = \mathbf{e}_r$ is the reflected wave direction for a plane wave interacting with a plane surface which coincides with the tangent plane of the surface. These fields are the values taken on the lit surface, C_{lit}, of the flaw where the incident waves can directly strike the surface. On the remaining part of the flaw surface the fields are assumed to be identically zero. However, the predominate scattering from the lit surface of a flaw comes from "specular" points where the incident and scattered wave directions satisfy Snell's law. Using Eq. 3.13 in Eq. 3.8 and noting that at the specular points $\mathbf{e}_r = -\mathbf{e}^{(2)}$, $(\mathbf{e}_{inc} \cdot \mathbf{n}) = -(\mathbf{e}_r \cdot \mathbf{n})$, and $\mathbf{e}_{scat} = \mathbf{e}_r$ [2], Eq. 3.7 can be rewritten as

$$\begin{aligned} V(\mathbf{X}_s, \mathbf{X}_r, \omega) =& s_I(\omega) \hat{P}^{(1)}(\mathbf{X}_s, \mathbf{X}_0, \omega) \hat{P}^{(2)}(\mathbf{X}_r, \mathbf{X}_0, \omega) \\ & \cdot \frac{2\rho c}{l_A \rho_2 c_2} \int_{C_{lit}} R_{23}(\mathbf{e}_r \cdot \mathbf{n}) \exp[ik_2(\mathbf{e}^{(1)} + \mathbf{e}^{(2)}) \cdot (\mathbf{X} - \mathbf{X}_0)] ds(\mathbf{X}). \end{aligned} \tag{3.15}$$

Eq. 3.15 will be the starting point for the development of the quantitative imaging algorithm.

www.manaraa.com

Quantitative pulse-echo imaging algorithm

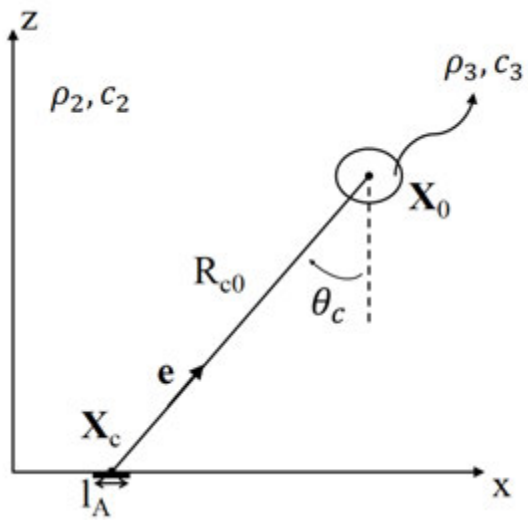

Figure 3.2: Geometry for using a single element in pulse-echo.

For a pulse-echo inspection setup in a single medium whose density and wavespeed are ρ_2 and c_2, respectively, take $\rho = \rho_1 = \rho_2$, $c = c_1 = c_2$, $\mathbf{X}_r = \mathbf{X}_s = \mathbf{X}_c$, $\hat{P}^{(1)} = \hat{P}^{(2)} = \hat{P}(\mathbf{X}_c, \mathbf{X}_0, \omega)$, $\mathbf{e}_r \cdot \mathbf{n} = 1$, and $\mathbf{e}^{(1)} = \mathbf{e}^{(2)} = \mathbf{e}$ and Eq. 3.15 can be written as

$$V(\mathbf{X}_c, \omega) = s_I(\omega)[\hat{P}(\mathbf{X}_c, \mathbf{X}_0, \omega)]^2 \frac{2}{l_A} \int_{C_{lit}} R_{23} \exp[2ik_2 \mathbf{e} \cdot \mathbf{X}'] ds(\mathbf{X}') \tag{3.16}$$

where $\mathbf{X}' = \mathbf{X} - \mathbf{X}_0$ is a 2-D position vector with $\mathbf{X}' = (x', z')$ measured from the "flaw center" $\mathbf{X}_0 = (x_0, z_0)$. The pressure $\hat{P}(\mathbf{X}_c, \mathbf{X}_0, \omega)$ is the normalized pressure from an incident wave at point $\mathbf{X}_0$ from an element whose centroid is at $\mathbf{X}_c$:

$$\hat{P}(\mathbf{X}_c, \mathbf{X}_0, \omega) = \frac{P(\mathbf{X}_c, \mathbf{X}_0, \omega)}{\rho_1 c_1 v_T^{(1)}} \exp[i\omega T(\mathbf{X}_c, \mathbf{X}_0)]. \tag{3.17}$$

Setting $\mathbf{k} = 2k_2\mathbf{e}$ and allowing the element centroid to vary over all $\mathbf{X}_c = (x_c, 0)$ along $z = 0$ and letting C be the part of the flaw surface from which elements along this line can receive all specular responses gives

$$V(\mathbf{X}_c, \omega) = s_I(\omega)[\hat{P}(\mathbf{X}_c, \mathbf{X}_0, \omega)]^2 \frac{2}{l_A} \int_{C} R_{23} \exp[i\mathbf{k} \cdot \mathbf{X}'] ds(\mathbf{X}'). \tag{3.18}$$

www.manaraa.com

We can rewrite Eq. 3.18 by introducing a singularity function, $\gamma_C(\mathbf{X}')$, with the property

$$\int_C f(\mathbf{X}')ds(\mathbf{X}') = \int \gamma_C(\mathbf{X}')f(\mathbf{X}')dA(\mathbf{X}') \tag{3.19}$$

which gives

$$V(\mathbf{X}_c,\omega) = s_I(\omega)[\hat{P}(\mathbf{X}_c,\mathbf{X}_0,\omega)]^2\frac{2}{l_A}\int R_{23}\gamma_C(\mathbf{X}')\exp[i\mathbf{k}\cdot\mathbf{X}']dA(\mathbf{X}'). \tag{3.20}$$

If we define the reflectivity, $\mathscr{R}$, as

$$\mathscr{R}(\mathbf{X}') \equiv R_{23}\gamma_C(\mathbf{X}') \tag{3.21}$$

we can write its 2-D Fourier transform as

$$\overline{\mathscr{R}}(\mathbf{k}) = \int R_{23}\gamma_C(\mathbf{X}')\exp[i\mathbf{k}\cdot\mathbf{X}']dA(\mathbf{X}'). \tag{3.22}$$

Inverting Eq. 3.22 gives

$$R_{23}\gamma_C(\mathbf{X}') = \frac{1}{4\pi^2}\int \overline{\mathscr{R}}(\mathbf{k})\exp[-i\mathbf{k}\cdot\mathbf{X}']d^2\mathbf{k}. \tag{3.23}$$

Eq. 3.22 allows Eq. 3.20 to be written as

$$V(\mathbf{X}_c,\omega) = s_I(\omega)[\hat{P}(\mathbf{X}_c,\mathbf{X}_0,\omega)]^2\frac{2}{l_A}\overline{\mathscr{R}}(\mathbf{k}) \tag{3.24}$$

or, when rearranged,

$$\overline{\mathscr{R}}(\mathbf{k}) = \frac{l_A V(\mathbf{X}_c,\omega)}{2s_I(\omega)[\hat{P}(\mathbf{X}_c,\mathbf{X}_0,\omega)]^2}. \tag{3.25}$$

Substituting Eq. 3.25 into Eq. 3.23 gives an equation for an image of the reflectivity as

$$I_{\mathscr{R}}(\mathbf{X}') \equiv R_{23}\gamma_C(\mathbf{X}') = \frac{l_A}{8\pi^2}\int \frac{V(\mathbf{X}_c,\omega)}{s_I(\omega)[\hat{P}(\mathbf{X}_c,\mathbf{X}_0,\omega)]^2}\exp[-i\mathbf{k}\cdot\mathbf{X}']d^2\mathbf{k}. \tag{3.26}$$

The division present is unstable at high frequencies, so a Wiener filter can be implemented [25] as

$$V_W(\mathbf{X}_c,\mathbf{X}_0,\omega) = \frac{V(\mathbf{X}_c,\omega)\left(s_I(\omega)[\hat{P}(\mathbf{X}_c,\mathbf{X}_0,\omega)]^2\right)^*}{\left|s_I(\omega)[\hat{P}(\mathbf{X}_c,\mathbf{X}_0,\omega)]^2\right|^2 + \varepsilon^2 max\left(\left|s_I(\omega)[\hat{P}(\mathbf{X}_c,\mathbf{X}_0,\omega)]^2\right|^2\right)} \tag{3.27}$$

www.manaraa.com

where the asterisk denotes the complex conjugate and ε is a noise constant. Substituting $V_W(\mathbf{X}_c, \mathbf{X}_0, \omega)$ into Eq. 3.26 gives

$$I_{\mathscr{R}}(\mathbf{X}') = \frac{l_A}{8\pi^2} \int V_W(\mathbf{X}_c, \mathbf{X}_0, \omega) \exp[-i\mathbf{k} \cdot \mathbf{X}'] d^2\mathbf{k}. \tag{3.28}$$

Changing the integration variables gives

$$I_{\mathscr{R}}(\mathbf{X}') = \frac{l_A}{8\pi^2} \int V_W(\mathbf{X}_c, \mathbf{X}_0, \omega) \exp[-i\mathbf{k} \cdot \mathbf{X}'] \left| \frac{(\partial k_x, \partial k_z)}{(\partial \omega, \partial \theta_c)} \right| d\omega d\theta_c \tag{3.29}$$

where the Jacobian is

$$\begin{aligned} \left| \frac{\partial(k_x, k_z)}{\partial(\omega, \theta_c)} \right| &= \left| det \begin{pmatrix} \frac{\partial k_x}{\partial \omega} & \frac{\partial k_z}{\partial \omega} \\ \frac{\partial k_x}{\partial \theta_c} & \frac{\partial k_z}{\partial \theta_c} \end{pmatrix} \right| \\ &= \left| det \begin{bmatrix} -2\sin\theta_c/c & 2\cos\theta_c/c \\ -2\omega\cos\theta_c/c & -2\omega\sin\theta_c/c \end{bmatrix} \right| \\ &= 4\,|\omega|\,/c^2. \end{aligned} \tag{3.30}$$

The integration on θ_c can be written in terms of x_c for $z = 0$ because

$$d\theta_c = \cos\theta_c \frac{dx_c}{R_{c0}}. \tag{3.31}$$

Using Eqs. 3.30 and 3.31 in Eq. 3.29 gives

$$I_{\mathscr{R}}(\mathbf{X}') = \frac{l_A}{2\pi^2 c^2} \int \frac{\cos\theta_c}{R_{c0}} V_W(\mathbf{X}_c, \mathbf{X}_0, \omega) \exp[-i\mathbf{k} \cdot \mathbf{X}'] \,|\omega|\, d\omega dx_c, \tag{3.32}$$

and using M discrete frequencies with spacing Δf and N discrete element locations with pitch (spacing from one element centroid to the next) Δx_c, Eq. 3.32 can be written as

$$I^{BA}_{\mathscr{R}}(\mathbf{X}') = \frac{2 l_A \Delta f \Delta x_c}{c^2} 2\,\mathrm{Re} \left(\sum_{m=1}^{M} \sum_{n=1}^{N} \frac{(\cos\theta_c)_n}{(R_{c0})_n} f_m V_W(\mathbf{X}_{cn}, \mathbf{X}_0, \omega_m) \exp[-i\mathbf{k}_{mn} \cdot \mathbf{X}'] \right), \tag{3.33}$$

where the *BA* superscript denotes that this is the band- and aperture-limited form of Eq. 3.32. Eqs. 3.32 and 3.33 are the pulse-echo versions of the continuous and discrete quantitative imaging algorithm.

www.manaraa.com

Relation to physical optics far-field inverse scattering

Eq. 3.24 is very similar to the physical optics far-field inverse scattering (POFFIS) identity, which relates the reflectivity of a scatterer to the scattered field [4, 17, 18]. The POFFIS identity assumes that there is infinite bandwidth and that the incident field is from a concentrated source with no directivity. The pressure field from a concentrated line source can be written as

$$\hat{P}(\mathbf{X}_c, \mathbf{X}_0, \omega) = \sqrt{\frac{2k_2}{i\pi}} \frac{l_A}{2} \frac{\exp(ik_2 R_{c0})}{\sqrt{R_{c0}}} D(\theta_c, \omega) \tag{3.34}$$

where $D(\theta_c, \omega)$ is the far-field directivity [26]. Placing this result in Eq. 3.24 gives

$$V(\mathbf{X}_c, \omega) = s_I(\omega) \frac{2k_2}{i\pi} \frac{l_A}{2} \frac{\exp(2ik_2 R_{c0})}{R_{c0}} [D(\theta_c, \omega)]^2 \overline{\mathscr{R}}(\mathbf{k}) \tag{3.35}$$

which is the 2-D version of the POFFIS identity with the system function and far-field directivities retained. However, here the identity is relating the reflectivity to the actual measured voltage rather than to the scattered pressure wavefield present in POFFIS. Inverting Eq. 3.35 to get

$$I_{\mathscr{R}}(\mathbf{X}') = \frac{c_2}{4\pi l_A} \int \frac{R_{c0} V(\mathbf{X}_c, \omega)}{-i\omega s_I(\omega) [D(\theta_c, \omega)]^2} \exp(-2ik_2 R_{c0} - 2ik_2 \mathbf{e} \cdot \mathbf{X}') d^2\mathbf{k} \tag{3.36}$$

provides an opportunity to gain insight into what the quantitative imaging algorithm of Eq. 3.26 is correcting for. The R_{c0} term in Eq. 3.36 is correcting for amplitude loss due to wave propagation: from the element to the flaw there will be an amplitude decay of $1/\sqrt{R_{c0}}$, and from the flaw back to the element there will be another decay of $1/\sqrt{R_{c0}}$. The $[D(\theta_c, \omega)]^2$ term corrects for the directivity in transmission and reception, and the system function, $s_I(\omega)$, corrects for the ultrasonic system effects. The POFFIS formulation includes the amplitude term but neglects the system function and directivity effects, both of which are important in order to model actual NDE measurement systems.

www.manaraa.com

Quantitative full matrix imaging algorithm

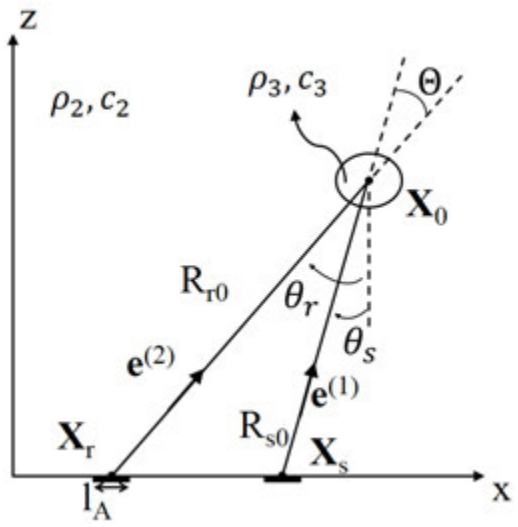

Figure 3.3: Geometry for sending on one element and receiving on another.

Returning to Eq. 3.15, which can be written for a single medium as

$$V(\mathbf{X}_s,\mathbf{X}_r,\omega) = s_I(\omega)\hat{P}^{(1)}(\mathbf{X}_s,\mathbf{X}_0,\omega)\hat{P}^{(2)}(\mathbf{X}_r,\mathbf{X}_0,\omega) \cdot \frac{2\rho c}{l_A\rho_2 c_2}\int_{C_{lit}} R_{23}(\mathbf{e}_r\cdot\mathbf{n})\exp[ik_2(\mathbf{e}^{(1)}+\mathbf{e}^{(2)})\cdot(\mathbf{X}-\mathbf{X}_0)]ds(\mathbf{X}), \tag{3.37}$$

an equation for an image that uses all combinations of pitch-catch signals can be developed in the same way as the pulse-echo case. Defining the reflectivity now as

$$\mathscr{R} \equiv R_{23}(\mathbf{e}_r\cdot\mathbf{n})\gamma_C(\mathbf{X}') \tag{3.38}$$

and setting

$$\mathbf{k} = k_2(\mathbf{e}^{(1)}+\mathbf{e}^{(2)}) \tag{3.39}$$

the Fourier transform of the reflectivity can be written as

$$\overline{\mathscr{R}}(\mathbf{k}) = \int R_{23}(\mathbf{e}_r\cdot\mathbf{n})\gamma_C(\mathbf{X}')\exp[i\mathbf{k}\cdot\mathbf{X}']dA(\mathbf{X}'). \tag{3.40}$$

www.manaraa.com

Now, the measured voltage signal can be again written in terms of the Fourier transform of the reflectivity as

$$V(\mathbf{X}_s,\mathbf{X}_r,\omega) = s_I(\omega)\hat{P}^{(1)}(\mathbf{X}_s,\mathbf{X}_0,\omega)\hat{P}^{(2)}(\mathbf{X}_r,\mathbf{X}_0,\omega)\frac{2}{l_A}\overline{\mathscr{R}}(\mathbf{k}). \tag{3.41}$$

Doing an inverse Fourier transform on Eq. 3.41 gives

$$I_{\mathscr{R}}(\mathbf{X}') \equiv R_{23}(\mathbf{e}_r\cdot\mathbf{n})\gamma_C(\mathbf{X}') = \frac{l_A}{8\pi^2}\int \frac{V(\mathbf{X}_s,\mathbf{X}_r,\omega)}{s_I(\omega)\hat{P}^{(1)}(\mathbf{X}_s,\mathbf{X}_0,\omega)\hat{P}^{(2)}(\mathbf{X}_r,\mathbf{X}_0,\omega)}\exp[-i\mathbf{k}\cdot\mathbf{X}']d^2\mathbf{k}. \tag{3.42}$$

First, we will consider the case where we hold the sending element fixed but allow the receiving element to vary. This is called the "common shot" case in seismology. For this case we can consider $\mathbf{k}$ to be a function of ω and θ_r. With a change of variables, Eq. 3.42 can be rewritten as

$$\begin{aligned} I_{\mathscr{R}}(\mathbf{X}') \equiv R_{23}(\mathbf{e}_r\cdot\mathbf{n})\gamma_C(\mathbf{X}') = \frac{l_A}{8\pi^2}\int &\frac{V(\mathbf{X}_s,\mathbf{X}_r,\omega)}{s_I(\omega)\hat{P}^{(1)}(\mathbf{X}_s,\mathbf{X}_0,\omega)\hat{P}^{(2)}(\mathbf{X}_r,\mathbf{X}_0,\omega)} \\ &\cdot\exp[-i\mathbf{k}\cdot\mathbf{X}']\left|\frac{\partial(\mathbf{k})}{\partial(\omega,\theta_r)}\right| d\omega d\theta_r. \end{aligned} \tag{3.43}$$

Here the Jacobian is

$$\begin{aligned} \left|\frac{\partial(\mathbf{k})}{\partial(\omega,\theta_r)}\right| &= \left|\frac{\omega}{c^2}\det\begin{bmatrix}\mathbf{e}^{(1)}+\mathbf{e}^{(2)} \\ \partial\mathbf{e}^{(2)}/\partial\theta_r\end{bmatrix}\right| = \left|\frac{\omega}{c^2}\mathbf{j}\cdot\left[(\mathbf{e}^{(1)}+\mathbf{e}^{(2)})\times\frac{\partial\mathbf{e}^{(2)}}{\partial\theta_r}\right]\right| \\ &= \left|\frac{\omega}{c^2}(\mathbf{e}^{(1)}+\mathbf{e}^{(2)})\cdot\left[\frac{\partial\mathbf{e}^{(2)}}{\partial\theta_r}\times\mathbf{j}\right]\right| \end{aligned} \tag{3.44}$$

where the distributional property of the triple product has been used. Now, for the 2-D case presented here, $\frac{\partial\mathbf{e}^{(2)}}{\partial\theta_r}\times\mathbf{j} = -\mathbf{e}^{(2)}$, which gives

$$\left|\frac{\partial(\mathbf{k})}{\partial(\omega,\theta_r)}\right| = \left|\frac{\omega}{c^2}(\mathbf{e}^{(1)}+\mathbf{e}^{(2)})\cdot\left[-\mathbf{e}^{(2)}\right]\right| = \left|\frac{-\omega}{c^2}\left(\mathbf{e}^{(1)}\cdot\mathbf{e}^{(2)}+\mathbf{e}^{(2)}\cdot\mathbf{e}^{(2)}\right)\right|. \tag{3.45}$$

Noting that the sign goes away because of the absolute value and taking $\mathbf{e}^{(1)}\cdot\mathbf{e}^{(2)} = \cos\Theta$ and $\mathbf{e}^{(2)}\cdot\mathbf{e}^{(2)} = 1$ gives the Jacobian as

$$\left|\frac{\partial(\mathbf{k})}{\partial(\omega,\theta_r)}\right| = \left|\frac{\omega}{c^2}(1+\cos\Theta)\right|. \tag{3.46}$$

www.manaraa.com

Using Eq. 3.46 in Eq. 3.43 gives

$$I_{\mathscr{R}}(\mathbf{X}') = \frac{l_A}{8\pi^2}\int\left|\frac{\omega}{c^2}(1+\cos\Theta)\right|\frac{V(\mathbf{X}_s,\mathbf{X}_r,\omega)}{s_I(\omega)\hat{P}^{(1)}(\mathbf{X}_s,\mathbf{X}_0,\omega)\hat{P}^{(2)}(\mathbf{X}_r,\mathbf{X}_0,\omega)} \cdot\exp[-i\mathbf{k}\cdot\mathbf{X}']d\omega d\theta_r. \tag{3.47}$$

As with the pulse-echo case, the integration on θ_r can be changed to an integration over x_r because $dx_r = R_{r0}d\theta_r/\cos\theta_r$, giving

$$I_{\mathscr{R}}(\mathbf{X}') = \frac{l_A}{8\pi^2}\int\left|\frac{\omega}{c^2}(1+\cos\Theta)\right|\frac{\cos\theta_r}{R_{r0}}\frac{V(\mathbf{X}_s,\mathbf{X}_r,\omega)}{s_I(\omega)\hat{P}^{(1)}(\mathbf{X}_s,\mathbf{X}_0,\omega)\hat{P}^{(2)}(\mathbf{X}_r,\mathbf{X}_0,\omega)} \cdot\exp[-i\mathbf{k}\cdot\mathbf{X}']d\omega dx_r. \tag{3.48}$$

Since the sending element was held fixed, Eq. 3.48 is the equation for an image formed for a fixed angle of incidence; that is to say, $I_{\mathscr{R}}(\mathbf{X}') = I_{\mathscr{R}}(\mathbf{X}',\theta_s)$. If we now let the sending element vary, we can form up an image that is the integral over these angles of incidence, i.e.

$$I'_{\mathscr{R}}(\mathbf{X}') = \int I_{\mathscr{R}}(\mathbf{X}',\theta_s)d\theta_s. \tag{3.49}$$

The integration on θ_s can be written as an integration on x_s because $dx_s = R_{s0}d\theta_s/\cos\theta_s$, giving a full matrix image defined as

$$I'_{\mathscr{R}}(\mathbf{X}') = \int I_{\mathscr{R}}d\theta_s = \int\frac{\cos\theta_s}{R_{s0}}I_{\mathscr{R}}dx_s. \tag{3.50}$$

Placing Eq. 3.48 into Eq. 3.50 gives

$$I'_{\mathscr{R}}(\mathbf{X}') = \frac{l_A}{8\pi^2}\int\left|\frac{\omega}{c^2}(1+\cos\Theta)\right|\frac{\cos\theta_s}{R_{s0}}\frac{\cos\theta_r}{R_{r0}}\frac{V(\mathbf{X}_s,\mathbf{X}_r,\omega)}{s_I(\omega)\hat{P}^{(1)}(\mathbf{X}_s,\mathbf{X}_0,\omega)\hat{P}^{(2)}(\mathbf{X}_r,\mathbf{X}_0,\omega)} \cdot\exp[-i\mathbf{k}\cdot\mathbf{X}']d\omega dx_r dx_s \tag{3.51}$$

which is our continuous full-matrix quantitative imaging equation. Using M discrete frequencies, N discrete transmission elements, and N discrete receiving elements with spacings Δf, Δx_s, and Δx_r, respectively, gives

$$I'^{BA}_{\mathscr{R}}(\mathbf{X}') = \frac{l_A\Delta f\Delta x_s\Delta x_r}{4\pi}2\,\mathrm{Re}\sum_{m=1}^{M}\sum_{n=1}^{N}\sum_{l=1}^{N}\left|\frac{\omega_m}{c^2}(1+\cos\Theta_{nl})\right|\frac{(\cos\theta_s)_n}{(R_{s0})_n}\frac{(\cos\theta_r)_l}{(R_{r0})_l} \cdot\frac{V(\mathbf{X}_{sn},\mathbf{X}_{rl},\omega_m)}{s_I(\omega_m)\hat{P}^{(1)}(\mathbf{X}_{sn},\mathbf{X}_0,\omega_m)\hat{P}^{(2)}(\mathbf{X}_{rl},\mathbf{X}_0,\omega_m)}\exp[-i\mathbf{k}_{mnl}\cdot\mathbf{X}']. \tag{3.52}$$

www.manaraa.com

As with the pulse-echo case, the division present is unstable at high frequencies, so a Wiener filter can be implemented as

$$V_W(\mathbf{X}_s,\mathbf{X}_r,\mathbf{X}_0,\omega) = \frac{V(\mathbf{X}_s,\mathbf{X}_r,\omega)\left(s_I(\omega)\hat{P}^{(1)}(\mathbf{X}_s,\mathbf{X}_0,\omega)\hat{P}^{(2)}(\mathbf{X}_r,\mathbf{X}_0,\omega)\right)^*}{\left|s_I(\omega)\hat{P}^{(1)}(\mathbf{X}_s,\mathbf{X}_0,\omega)\hat{P}^{(2)}(\mathbf{X}_r,\mathbf{X}_0,\omega)\right|^2+\varepsilon^2\max\left(\left|s_I(\omega)\hat{P}^{(1)}(\mathbf{X}_s,\mathbf{X}_0,\omega)\hat{P}^{(2)}(\mathbf{X}_r,\mathbf{X}_0,\omega)\right|^2\right)}. \tag{3.53}$$

Using Eq. 3.53 in Eqs. 3.51 and 3.52 gives Eqs. 3.54 and 3.55

$$I'_{\mathscr{R}}(\mathbf{X}') = \frac{l_A}{8\pi^2}\int\left|\frac{\omega}{c^2}(1+\cos\Theta)\right|\frac{\cos\theta_s}{R_{s0}}\frac{\cos\theta_r}{R_{r0}}V_W(\mathbf{X}_s,\mathbf{X}_r,\mathbf{X}_0,\omega) \cdot\exp[-i\mathbf{k}\cdot\mathbf{X}']d\omega dx_r dx_s \tag{3.54}$$

$$I'^{BA}_{\mathscr{R}}(\mathbf{X}') = \frac{l_A\Delta f\Delta x_s\Delta x_r}{4\pi}2\,\mathrm{Re}\sum_{m=1}^{M}\sum_{n=1}^{N}\sum_{l=1}^{N}\left|\frac{\omega_m}{c^2}(1+\cos\Theta_{nl})\right|\frac{(\cos\theta_s)_n}{(R_{s0})_n}\frac{(\cos\theta_r)_l}{(R_{r0})_l} \cdot V_W(\mathbf{X}_{sn},\mathbf{X}_{rl},\mathbf{X}_0,\omega_m)\exp[-i\mathbf{k}_{mnl}\cdot\mathbf{X}']. \tag{3.55}$$

Eq. 3.54 and its discrete counterpart Eq. 3.55 are suitable for forming quantitative images using measured voltage signals obtained experimentally.

Inclusion Simulations

Images can be formed using simulated data, which is useful in studying the imaging process in detail. First we note that Eq. 3.56 below (which was shown earlier as Eq. 3.7 and is the Thompson-Gray measurement model for 2-D scalar problems in terms of the far-field scattering amplitude) can be placed in our full matrix imaging model, Eq. 3.51, to write that model in terms of the far-field scattering amplitude.

$$V(\mathbf{X}_s,\mathbf{X}_r,\omega) = s_I(\omega)\hat{P}^{(1)}(\mathbf{X}_s,\mathbf{X}_0,\omega)\hat{P}^{(2)}(\mathbf{X}_r,\mathbf{X}_0,\omega)A(\mathbf{e}_{inc};\mathbf{e}_{scat}) \cdot\left[\frac{1}{-ik_2l_A}\frac{\rho c}{\rho_2c_2}\sqrt{-8\pi ik_2}\right]. \tag{3.56}$$

We find for the continuous case

$$I'_{\mathscr{R}}(\mathbf{X}') = \frac{1}{8\pi^2}\int\left|\frac{\omega}{c^2}(1+\cos\Theta)\right|\frac{\cos\theta_s}{R_{s0}}\frac{\cos\theta_r}{R_{r0}}\sqrt{\frac{8\pi c}{-i\omega}} \cdot A(\mathbf{e}_{inc};\mathbf{e}_{scat},\omega)\exp[-i\mathbf{k}\cdot\mathbf{X}']d\omega dx_r dx_s \tag{3.57}$$

www.manaraa.com

and for the discrete case

$$I'^{BA}_{\mathscr{R}}(\mathbf{X}') = \frac{\Delta f \Delta x_r \Delta x_s}{4\pi} 2 \,\mathrm{Re} \sum_{m=1}^{M} \sum_{n=1}^{N} \sum_{l=1}^{N} \left| \frac{\omega_m}{c^2}(1+\cos\Theta_{nl}) \right| \frac{(\cos\theta_s)_n}{(R_{s0})_n} \frac{(\cos\theta_r)_l}{(R_{r0})_l} \sqrt{\frac{8\pi c}{-i\omega_m}} \cdot A(\mathbf{e}_{inc}; \mathbf{e}_{scat}, \omega_m) \exp[-i\mathbf{k}_{mnl} \cdot \mathbf{X}'] . \tag{3.58}$$

Similarly, the imaging equations for pulse-echo in terms of the scattering amplitude can be written as

$$I_{\mathscr{R}}(\mathbf{X}') = \frac{1}{2\pi^2 c^2} \int \frac{\cos\theta_c}{R_{c0}} \sqrt{\frac{8\pi c}{-i\omega}} A(\mathbf{e}_{inc}; -\mathbf{e}_{inc}, \omega) \exp[-i\mathbf{k} \cdot \mathbf{X}'] \, |\omega| \, d\omega dx_c \tag{3.59}$$

and its discrete counterpart

$$I^{BA}_{\mathscr{R}}(\mathbf{X}') = \frac{\Delta f \Delta x_c}{\pi c^2} 2 \,\mathrm{Re} \sum_{m=1}^{M} \sum_{n=1}^{N} \frac{(\cos\theta_c)_n}{(R_{c0})_n} \sqrt{\frac{8\pi c}{-i\omega_m}} A(\mathbf{e}_{inc}; -\mathbf{e}_{inc}, \omega_m) \exp[-i\mathbf{k}_{mn} \cdot \mathbf{X}'] \, |\omega_m| \, . \tag{3.60}$$

These forms of our imaging models are useful since exact expressions for the far-field scattering amplitude can be obtained using the method of separation of variables for the cases of cylindrical and spherical inclusions [2, 26]. For example, the scattering amplitude for a cylindrical inclusion of radius a with density $\rho_{flaw} = \rho_f$ and wavenumber $k_{flaw} = k_f$ in a host material with density $\rho_{host} = \rho_h$ and wavenumber $k_{host} = k_h$ is

$$A = -\sqrt{\frac{2}{i\pi k_h}} \left(\frac{\Delta_2(0)}{\Delta_1(0)} + 2 \sum_{n=1}^{\infty} \frac{\Delta_2(n)}{\Delta_1(n)} (-1)^n \cos(n\Theta) \right) \tag{3.61}$$

where

$$\frac{\Delta_2(n)}{\Delta_1(n)} = \frac{\frac{k_f}{\rho_f} J_n(k_h a) \left(J_{n+1}(k_f a) - \frac{n}{k_f a} J_n(k_f a) \right) - J_n(k_f a) \frac{k_h}{\rho_h} \left(J_{n+1}(k_h a) - \frac{n}{k_h a} J_n(k_h a) \right)}{\frac{k_f}{\rho_f} H_n^{(1)}(k_h a) \left(J_{n+1}(k_f a) - \frac{n}{k_f a} J_n(k_f a) \right) - J_n(k_f a) \frac{k_h}{\rho_h} \left(H_{n+1}^{(1)}(k_h a) - \frac{n}{k_h a} H_n^{(1)}(k_h a) \right)} \tag{3.62}$$

and J_n is the Bessel function of the first kind and order n, $H_n^{(1)}$ is the Hankel function of the first kind and order n, and Θ is the angle between the incident and scattered wave directions. In contrast, the scattering amplitude for a spherical inclusion of radius a with density $\rho_{flaw} = \rho_f$ and wavenumber $k_{flaw} = k_f$ in a host material with density $\rho_{host} = \rho_h$ and wavenumber $k_{host} = k_h$ is

$$A = \frac{i}{k_h} \left(\sum_{n=0}^{\infty} (2n+1)(-1)^n \frac{\Delta_2(n)}{\Delta_1(n)} P_n(cos(\Theta)) \right) \tag{3.63}$$

www.manaraa.com

where

$$\frac{\Delta_2(n)}{\Delta_1(n)} = \frac{\frac{1}{\rho_f} j_n(k_h a)\left[k_f a j_{n+1}(k_f a) - n j_n(k_f a)\right] - \frac{1}{\rho_h} j_n(k_f a)\left[k_h a j_{n+1}(k_h a) - n j_n(k_h a)\right]}{\frac{1}{\rho_f} h_n^{(1)}(k_h a)\left[k_f a j_{n+1}(k_f a) - n j_n(k_f a)\right] - \frac{1}{\rho_h} j_n(k_f a)\left[k_h a h_{n+1}^{(1)}(k_h a) - n h_n^{(1)}(k_h a)\right]} \tag{3.64}$$

and j_n is the spherical Bessel function of the first kind and order n, $h_n^{(1)}$ is the spherical Hankel function of the first kind and order n, and Θ is the angle between the incident and scattered wave directions. P_n is the n^{th} Legendre polynomial. Since the models used here are scalar, they correspond to the physical case of a fluid inclusion in a fluid host material. This case is much simpler than those typically encountered in NDE inspections, but it is still valuable for studying the image formation process.

The imaging algorithm was developed using the Kirchhoff approximation and assumes any signals are specular reflections. However, the scattering amplitudes obtained through separation of variables are exact and therefore contain signals that are not limited to specular reflections. For weakly scattering inclusions, much of the sound energy will propagate through the flaw and there will be a reflection off of the back surface of the inclusion. Creep waves, which are waves that travel around the surface of the flaw while shedding sound energy, can also cause prominent signals. Other signals, such as those due to multiply reflected waves, are generally small.

To understand how signals from these different waves contribute to the images being formed it is first necessary to identify which signals correspond to what type of wave. To do this, simulated A-scans can be created by inverting Eqs. 3.61 and 3.63 into the time domain. Calculations were done over a very wide set of frequencies from 0-20 MHz with a Hanning (also known as cosine-squared) window taper applied from 10-20 MHz prior to inversion. Figs. 3.4a and 3.4b show backscatter A-scans for rigid cylindrical and spherical inclusions with 1mm radii in water. It can be seen that the rigid cylinder has a significant front surface signal and a very small creep wave signal. The rigid sphere also has a large front surface signal, and its creep signal is more significant than that of the cylindrical inclusion.

www.manaraa.com

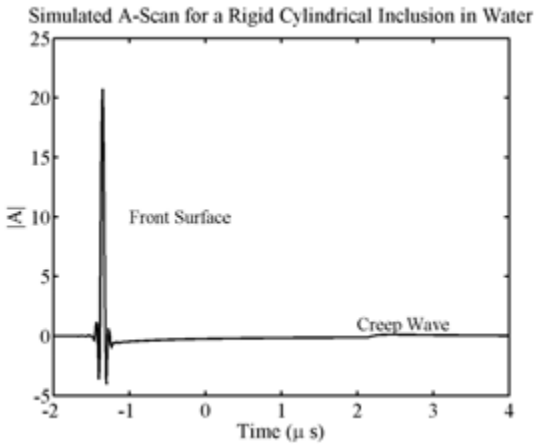

(a) Rigid cylindrical inclusion.

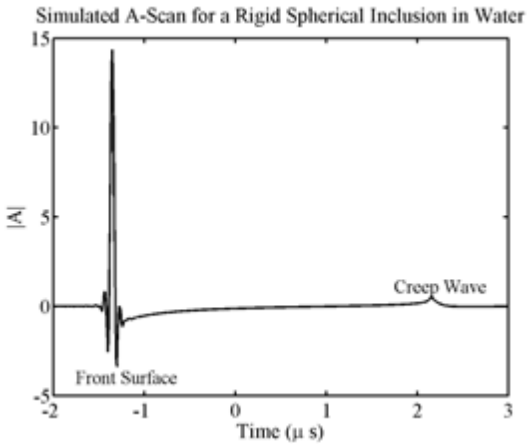

(b) Rigid spherical inclusion.

Figure 3.4: Simulated backscatter A-scans for rigid 1mm radius cylindrical and spherical inclusions in water.

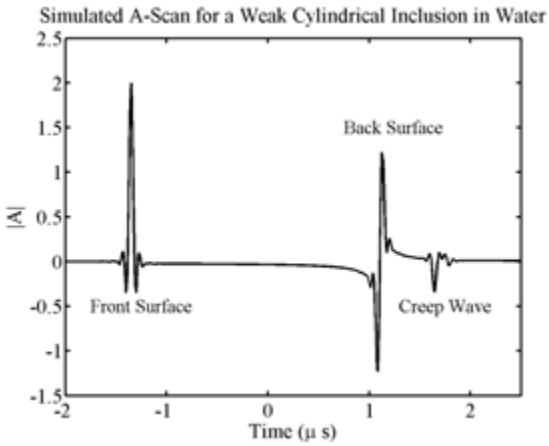

(a) Weakly scattering cylindrical inclusion.

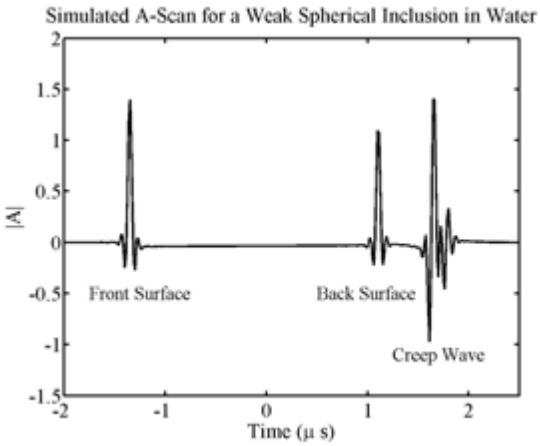

(b) Weakly scattering spherical inclusion.

Figure 3.5: Simulated backscatter A-scans for 1mm radius cylindrical and spherical inclusions in water. Inclusion wave speed and density 10% higher than those of water.

Figs. 3.5a and 3.5b show backscatter A-scans for weakly scattering cylindrical and spherical inclusions with 1mm radii in water. These inclusions, which have a ten percent increase in wave speed and density compared to water, have a front surface and creep wave signal along

www.manaraa.com

with a back surface signal. It is noteworthy that the back surface signal has a different structure depending on the inclusion shape. For the sphere, the back surface signal is a band-limited delta function (just like the front surface). For the cylinder, the back surface signal is the band-limited Hilbert transform of a delta function. When compared to the Born approximation, which assumes flaws are weakly scattering [2, 26], these results show good agreement. The creep wave signal for the spherical inclusion in Fig. 3.5b can be seen to be much more significant than that of the cylindrical inclusion in Fig. 3.5a. The spherical creep signal is larger than the back surface signal, which is not the case for the cylindrical inclusion. This is likely due to the fact that the creep wave around a cylindrical inclusion can only travel around paths that are about the axis of the cylinder. Creep waves around a spherical inclusion do not have this limitation, which means much more energy can be transmitted in the form of creep waves.

Sachse [27] and Frisk and Überall [28] have examined the signals scattered from cylindrical inclusions to determine what paths the signals traveled along. The signals from creep waves seen for 2-D inclusions whose wavespeeds are higher than that of the surrounding host material are consistent with a creep wave that travels around the path shown in Fig. 3.6b, which will be called the critical angle creep wave path. The angle θ is the critical angle determined by Snell's law for the host and flaw material: $\theta = \sin^{-1}\left(c_{host}/c_{flaw}\right)$. The vertical bars in Fig. 3.6a correspond to the times for the full width of the creep wave, since it is difficult to pick a single identifying feature, and the solid line in Fig. 3.6a is the predicted arrival time for creep waves following the path shown in Fig. 3.6b. It can be seen that the simulated creep wave signals follow the trend predicted for the critical angle creep wave.

www.manaraa.com

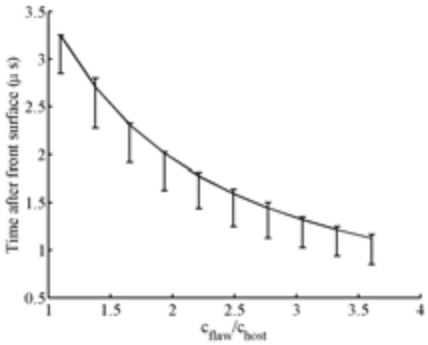

(a) Arrival times of creep wave (bars) compared to expected critical angle creep wave arrival time (solid line).

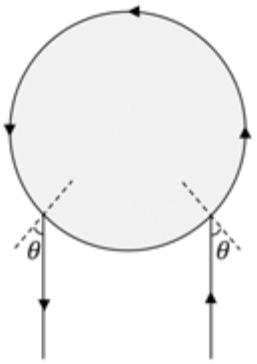

(b) Path of critical angle creep wave.

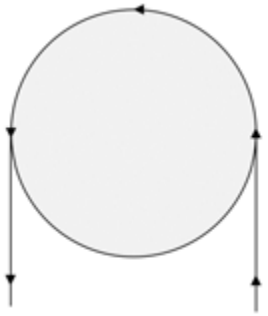

(c) Path of grazing creep wave.

Figure 3.6: Creep wave arrival times and paths.

When examining the A-scans for the rigid inclusions, Figs. 3.4a and 3.4b, it was found that the creep wave, which is notably almost non-existent for the cylindrical inclusion, occurs later in time than the critical angle creep wave. The arrival time of this creep wave is instead consistent with the path shown in Fig. 3.6c, which will be referred to as the grazing creep wave.

An understanding of the signals present in the simulated A-scans allows the transition to image formation to be made. To form images from simulated data using Eqs. 3.58 and 3.60, the locations of the array element centroids must be defined. The element centroids used here were those of a 32 element linear array with a 1mm pitch. The array is taken to be one

www.manaraa.com

inch (25.4mm) away from the center of the inclusion, making the centroid of the entire array located at $(x(mm), z(mm)) = (0, -25.4)$ in the coordinate system of the images. The point $(x(mm), z(mm)) = (0, 0)$ corresponds to the center of the flaw, with $(x(mm), z(mm)) = (0, -1)$ and $(x(mm), z(mm)) = (0, 1)$ being the locations of the front and back surfaces of the flaw, respectively.

Figure 3.7 shows pulse-echo and full matrix images for a 1mm radius cylindrical inclusion in water that has properties of $c_{flaw} = 1.5c_{host}$ and $\rho_{flaw} = 1.5\rho_{host}$.

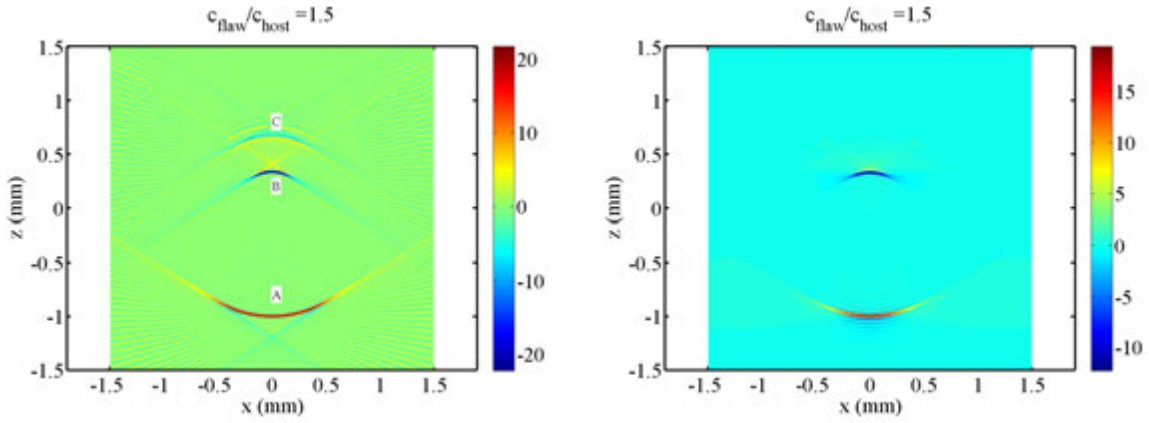

(a) Pulse-echo image.

(b) Full matrix image.

Figure 3.7: Simulated pulse-echo and full matrix images for a 1mm radius cylindrical inclusion in water. Flaw density and wave speed 50% higher than water.

Fig. 3.7a shows the pulse-echo image. The front surface (A), the back surface (B), and creep wave artifacts (C) can be seen, along with other artifacts that arise due to the fact that only N A-scans are being summed. It can be seen in Fig. 3.7b that using all combinations of pitch-catch (N^2 A-scans) to form the full matrix image does have an averaging effect as predicted by the imaging model; only the front and back surfaces are imaged. The large number of A-scans being summed effectively prevents the artifacts from becoming significant features in the image.

The front surface is being imaged in the correct location, but the back surface is not. For

www.manaraa.com

flaws whose wave speed are faster than the surrounding material, the back surface will be imaged within the flaw. This can be seen in Fig. 3.7a, where the back surface is imaged between the center of the flaw and where the back surface is actually located. This is because the imaging algorithm uses the wave speed of the host material in the time advances, so signals arising from waves that travel through the flaw, or around the flaw for the case of creep waves, will be not be imaged in the correct location. This can also be seen in Fig. 3.8.

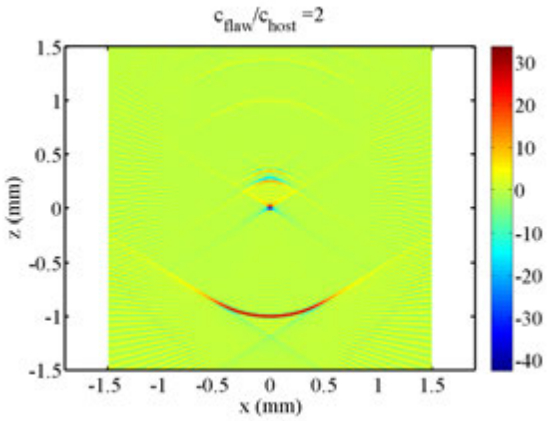

Figure 3.8: Simulated pulse-echo image for a 1mm radius cylindrical inclusion in water. Flaw density and wave speed twice those of water.

Figure 3.8 shows a pulse-echo image for a 1mm radius cylindrical inclusion in water that has properties of $c_{flaw} = 2c_{host}$ and $\rho_{flaw} = 2\rho_{host}$. Here, all of the back surface signals are advanced to the same point at the center of the flaw. The amplitude of this point in the image is greater than that of the front surface, even though there is no reflector there. This is an example of why it is important to understand how each signal can contribute in the image formation process.

To gain further insight into how the back surface and creep wave signals affect the image formation process, the amplitude at the flaw center can be observed for a range of flaw wave speeds. This is shown for the pulse-echo 1mm radius cylindrical case in Fig. 3.9a. The amplitude of the front surface is included for comparison in Fig. 3.9b.

www.manaraa.com

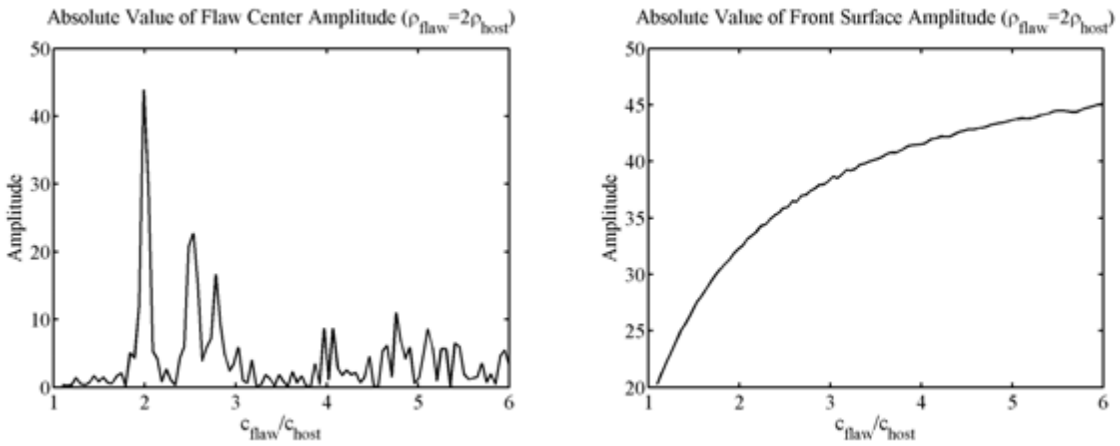

(a) Flaw center.

(b) Front surface.

Figure 3.9: Image amplitude at front surface and flaw center for a range of flaw wave speeds. Flaw is 1mm radius cylindrical inclusion in water, and the flaw density is held constant at $\rho_{flaw} = 2\rho_{host}$.

The flaw center amplitude is small until the peak at $c_{flaw} = 2c_{host}$, which is when the back surface signals are being imaged at the center. There is another large peak at approximately $c_{flaw} = 2.5c_{host}$ and a smaller peak shortly thereafter, which are likely due to the creep wave signals being focused at the center. There are a few smaller peaks for higher c_{flaw} values, which are likely caused by repeated echos of the back surface and creep wave signals.

The amplitude of the front surface, shown in Fig. 3.9b, is a measure of the reflectivity of the flaw surface. This reflectivity, defined in Eq. 3.21, is directly proportional to the reflection coefficient,

$$R = \frac{\rho_{flaw}c_{flaw} - \rho_{host}c_{host}}{\rho_{flaw}c_{flaw} + \rho_{host}c_{host}}, \tag{3.65}$$

for the interface between the host material and the flaw material. The proportionality depends on the band- and aperture-limiting of the system, as well as whether the pulse-echo or full matrix algorithm is used.

It is possible for flaws to have different combinations of density and wave speed but the same impedance, and therefore the same front surface amplitude. The wave speed of the flaw

www.manaraa.com

is responsible for the location of the back surface and creep wave artifacts, and the flaw density affects the relative amplitude of the features in the images. This can be seen in Fig. 3.10.

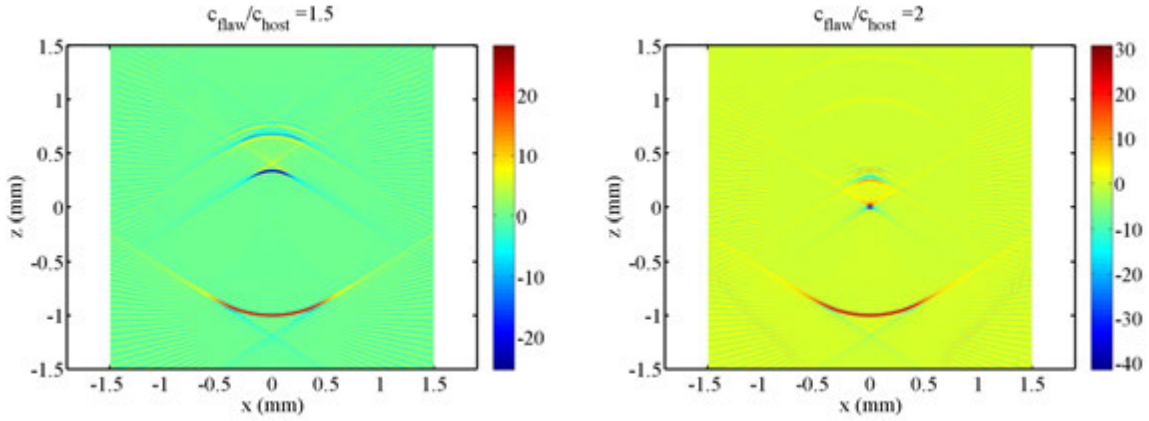

(a) $c_{flaw}/c_{host} = 1.5$, $\rho_{flaw}/\rho_{host} = 2$.

(b) $c_{flaw}/c_{host} = 2$, $\rho_{flaw}/\rho_{host} = 1.5$.

Figure 3.10: Simulated pulse-echo images for a 1mm radius cylindrical inclusion in water. Flaw density and wave speed differ but flaw impedance is the same.

Figure 3.10a shows a cylindrical inclusion with $c_{flaw} = 1.5c_{host}$ and $\rho_{flaw} = 2\rho_{host}$, while Fig. 3.10b shows the case for $c_{flaw} = 2c_{host}$ and $\rho_{flaw} = 1.5\rho_{host}$. These two cases have the same impedance, and, as expected, the front surface amplitudes are equal. The back surface and creep wave artifacts appear at different locations due to the difference in wave speed between the two flaws.

To show how changing flaw properties affects image formation, two appendices have been included. Appendix A shows a series of pulse-echo images for 1mm radius cylindrical inclusions in water for a range of flaw properties. Appendix B has a similar set of pulse-echo images for 1mm radius spherical inclusions in water.

www.manaraa.com

Conclusion

The algorithm presented here uses a model-based approach, which was shown to be a generalization of the POFFIS imaging method, to develop images that are quantitatively related to the properties of the scatterer present. The image formation process has corrections for the ultrasonic system and wave propagation effects built into the algorithm, rather than applying them in an ad-hoc fashion after the formation of the image. The different parts of the flaw response were matched with features in the images, and simulated data was used to show the quantitative nature of the images formed.

www.manaraa.com

CHAPTER 4. GENERAL CONLCLUSION

General Discussion

Ultrasonic phased arrays are a crucial technology for nondestructive evaluation. Their unique properties can be used to extend and advance traditional flaw characterization techniques, in addition to allowing new methods.

Building on the foundation of traditional time-of-flight diffraction sizing and equivalent flaw sizing, Chapter 2 shows, with experimental validation, how phased arrays can be used to estimate the size and orientation of isolated cracks. An explanation of how to extend this method to surface-breaking cracks and volumetric flaws is also presented. The size estimates provided by this method give much more quantitative information than other commonly used techniques, and the small flaws that were sized experimentally were estimated to within 20% of their actual values.

Chapter 3 advances the state of phased array imaging by first examining how the images are functions of the ultrasonic system, wave propagation, and the flaw. Corrections for the system and wave effects are then built into the imaging algorithm, making the images directly related to the properties of the flaw. Computer simulations of the image formation process with synthesized "exact" data verify the properties of this imaging method and explicitly define both what parts of the flaw response are imaged properly and what parts generate imaging artifacts.

www.manaraa.com

Future Research

In Chapter 2 sizing algorithms were introduced for isolated cracks, surface-breaking cracks, and volumetric flaws such as voids and inclusions. Only the isolated crack case had experimental validation. In the future, all three cases should be validated experimentally. The experimental sizing in Chapter 2 was done with a linear array, which is constrained in its beam steering capabilities. It would be useful to have a 2-D array that would allow full beam steering in 3-D so that one could obtain data in different directions without having to physically move the phased array.

Chapter 3 presented a quantitative model-based imaging algorithm and discussed that algorithm using simulated data for volumetric flaws. Practical tests of this method, using experimental data, should be done in the future to better define its advantages and limitations, particularly for dangerous flaws such as cracks.

www.manaraa.com

APPENDIX A. CYLINDRICAL INCLUSION IMAGES

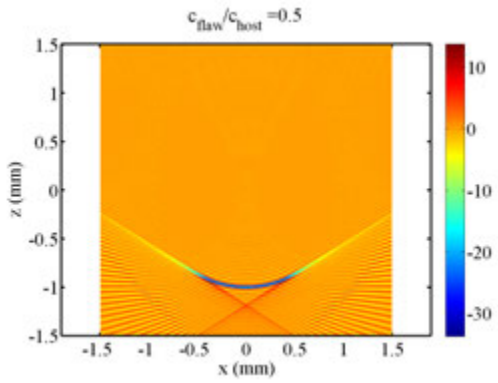

Figure A.1: $\frac{c_{flaw}}{c_{host}} = \frac{\rho_{flaw}}{\rho_{host}} = 0.50$

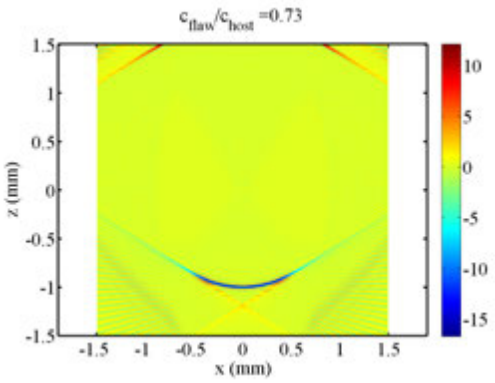

Figure A.2: $\frac{c_{flaw}}{c_{host}} = \frac{\rho_{flaw}}{\rho_{host}} = 0.73$

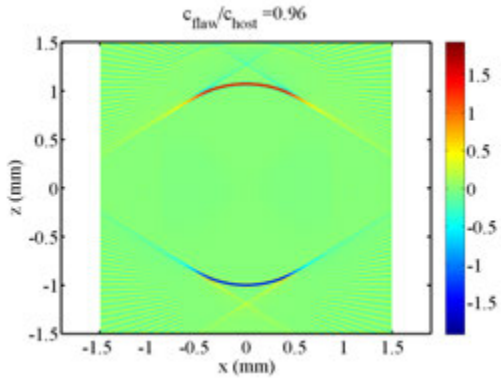

Figure A.3: $\frac{c_{flaw}}{c_{host}} = \frac{\rho_{flaw}}{\rho_{host}} = 0.96$

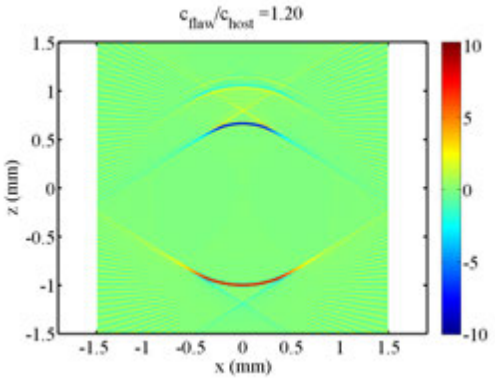

Figure A.4: $\frac{c_{flaw}}{c_{host}} = \frac{\rho_{flaw}}{\rho_{host}} = 1.20$

www.manaraa.com

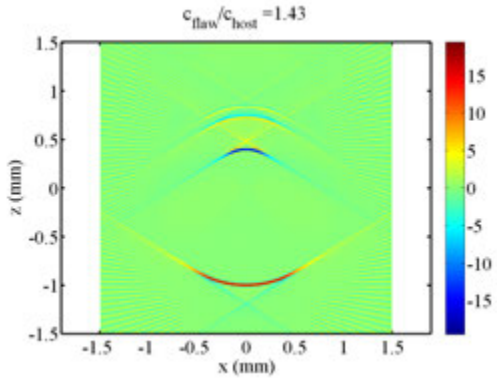

Figure A.5: $\frac{c_{flaw}}{c_{host}} = \frac{\rho_{flaw}}{\rho_{host}} = 1.43$

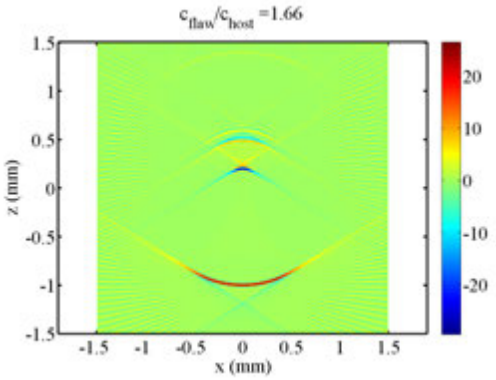

Figure A.6: $\frac{c_{flaw}}{c_{host}} = \frac{\rho_{flaw}}{\rho_{host}} = 1.66$

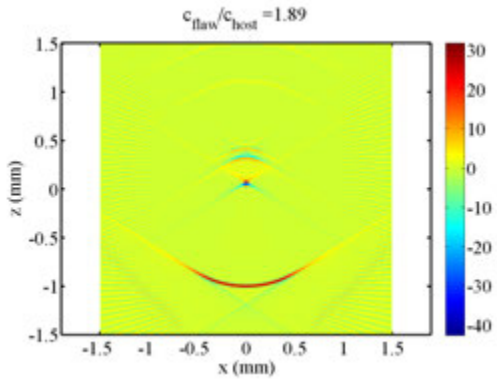

Figure A.7: $\frac{c_{flaw}}{c_{host}} = \frac{\rho_{flaw}}{\rho_{host}} = 1.89$

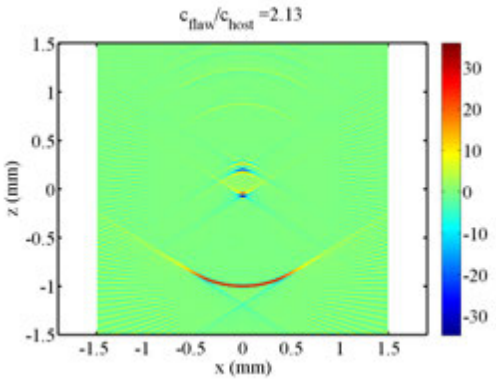

Figure A.8: $\frac{c_{flaw}}{c_{host}} = \frac{\rho_{flaw}}{\rho_{host}} = 2.13$

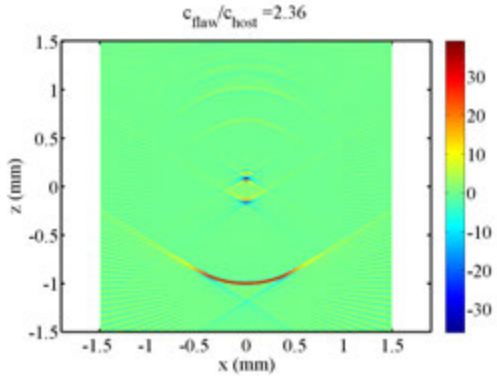

Figure A.9: $\frac{c_{flaw}}{c_{host}} = \frac{\rho_{flaw}}{\rho_{host}} = 2.36$

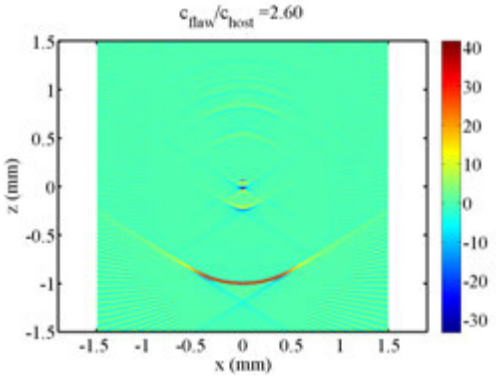

Figure A.10: $\frac{c_{flaw}}{c_{host}} = \frac{\rho_{flaw}}{\rho_{host}} = 2.60$

www.manaraa.com

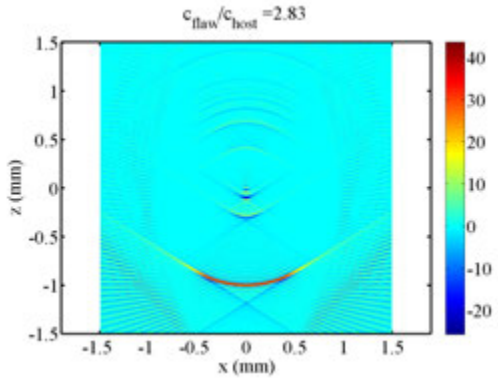

Figure A.11: $\frac{c_{flaw}}{c_{host}} = \frac{\rho_{flaw}}{\rho_{host}} = 2.83$

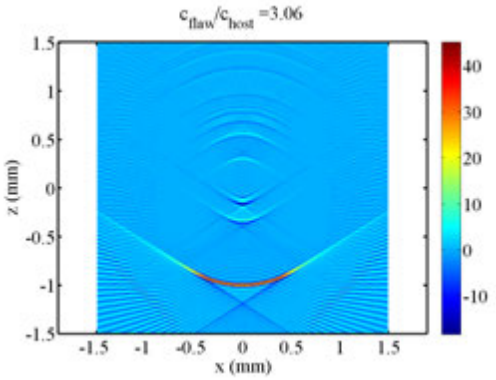

Figure A.12: $\frac{c_{flaw}}{c_{host}} = \frac{\rho_{flaw}}{\rho_{host}} = 3.06$

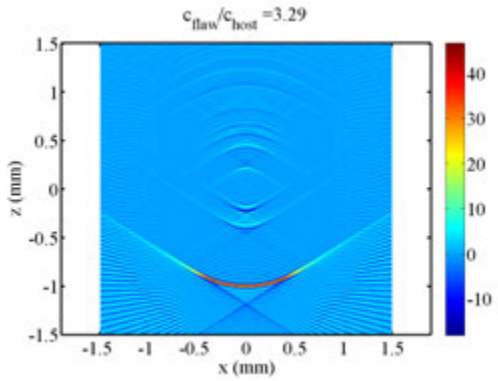

Figure A.13: $\frac{c_{flaw}}{c_{host}} = \frac{\rho_{flaw}}{\rho_{host}} = 3.29$

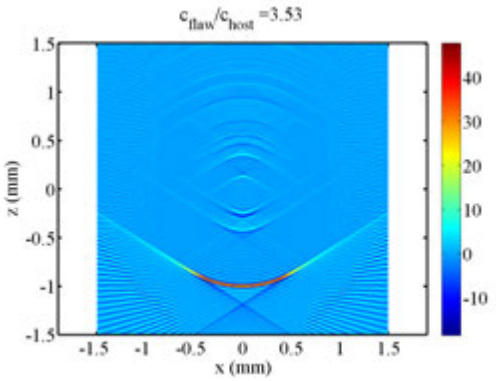

Figure A.14: $\frac{c_{flaw}}{c_{host}} = \frac{\rho_{flaw}}{\rho_{host}} = 3.53$

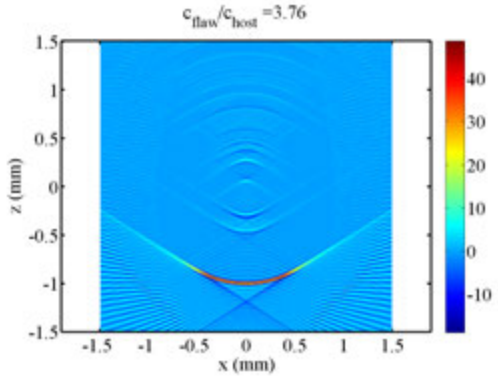

Figure A.15: $\frac{c_{flaw}}{c_{host}} = \frac{\rho_{flaw}}{\rho_{host}} = 3.76$

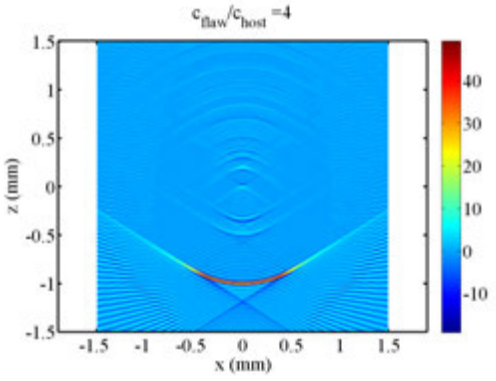

Figure A.16: $\frac{c_{flaw}}{c_{host}} = \frac{\rho_{flaw}}{\rho_{host}} = 4.00$

www.manaraa.com

APPENDIX B. SPHERICAL INCLUSION IMAGES

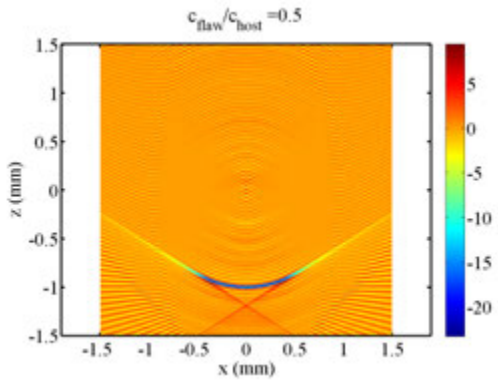

Figure B.1: $\frac{c_{flaw}}{c_{host}} = \frac{\rho_{flaw}}{\rho_{host}} = 0.50$

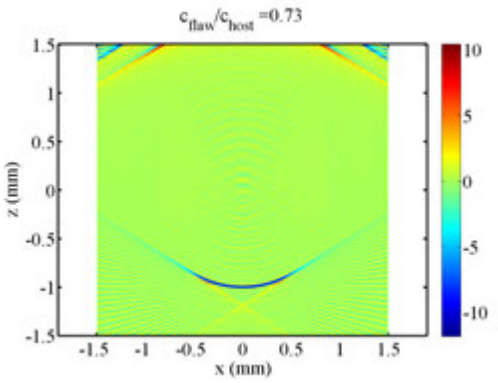

Figure B.2: $\frac{c_{flaw}}{c_{host}} = \frac{\rho_{flaw}}{\rho_{host}} = 0.73$

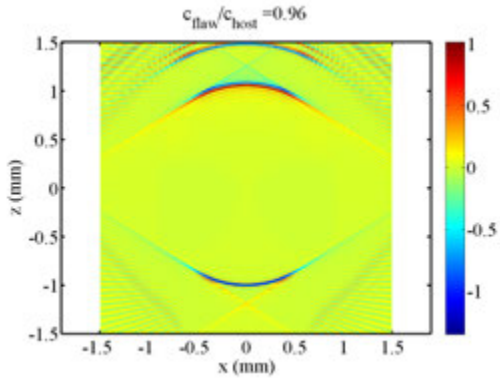

Figure B.3: $\frac{c_{flaw}}{c_{host}} = \frac{\rho_{flaw}}{\rho_{host}} = 0.96$

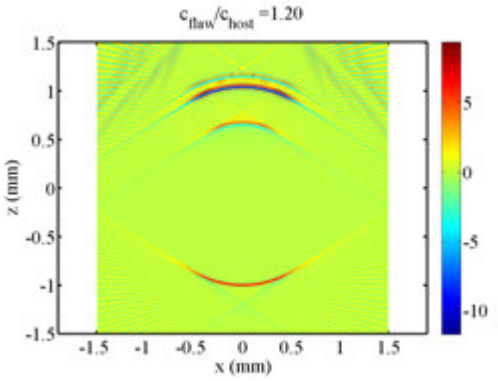

Figure B.4: $\frac{c_{flaw}}{c_{host}} = \frac{\rho_{flaw}}{\rho_{host}} = 1.20$

www.manaraa.com

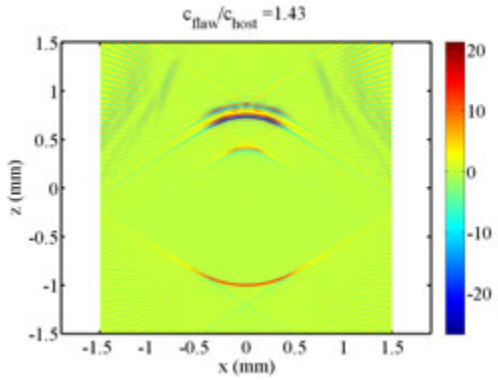

Figure B.5: $\frac{c_{flaw}}{c_{host}} = \frac{\rho_{flaw}}{\rho_{host}} = 1.43$

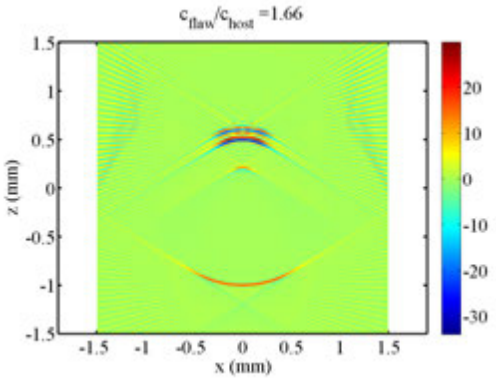

Figure B.6: $\frac{c_{flaw}}{c_{host}} = \frac{\rho_{flaw}}{\rho_{host}} = 1.66$

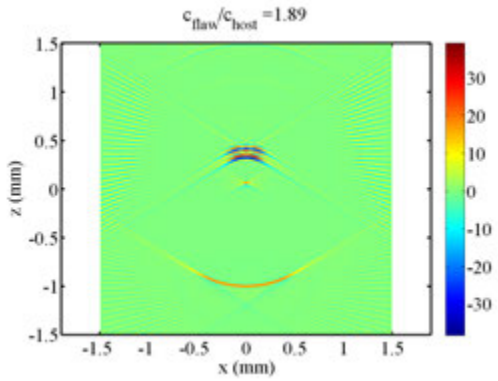

Figure B.7: $\frac{c_{flaw}}{c_{host}} = \frac{\rho_{flaw}}{\rho_{host}} = 1.89$

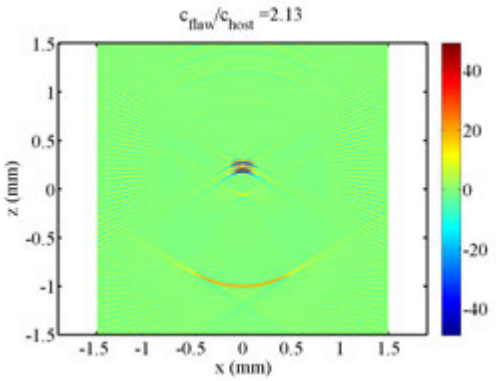

Figure B.8: $\frac{c_{flaw}}{c_{host}} = \frac{\rho_{flaw}}{\rho_{host}} = 2.13$

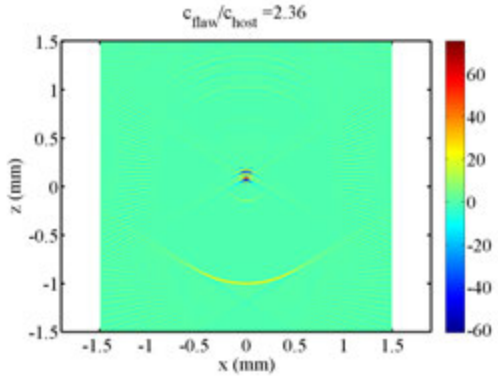

Figure B.9: $\frac{c_{flaw}}{c_{host}} = \frac{\rho_{flaw}}{\rho_{host}} = 2.36$

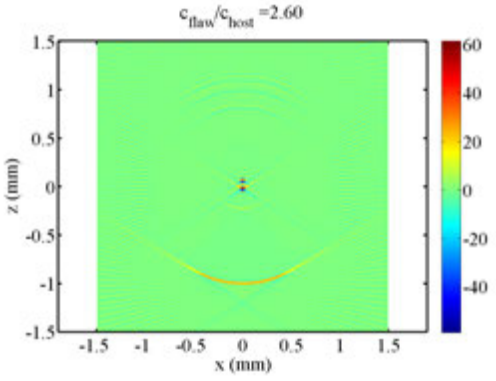

Figure B.10: $\frac{c_{flaw}}{c_{host}} = \frac{\rho_{flaw}}{\rho_{host}} = 2.60$

www.manaraa.com

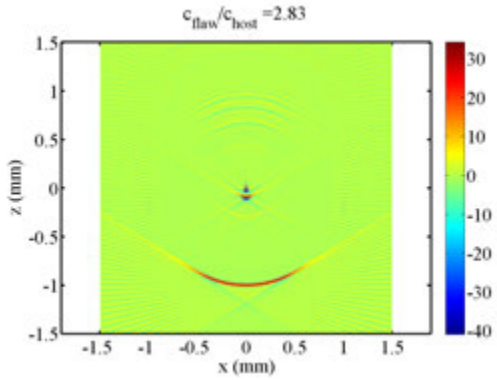

Figure B.11: $\frac{c_{flaw}}{c_{host}} = \frac{\rho_{flaw}}{\rho_{host}} = 2.83$

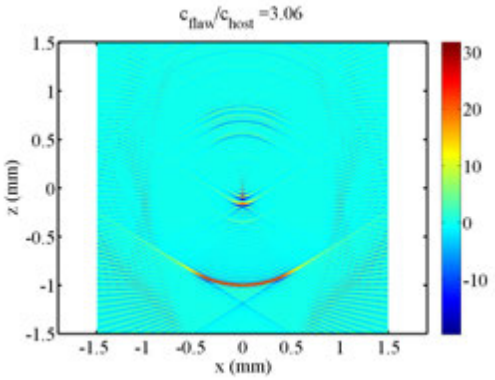

Figure B.12: $\frac{c_{flaw}}{c_{host}} = \frac{\rho_{flaw}}{\rho_{host}} = 3.06$

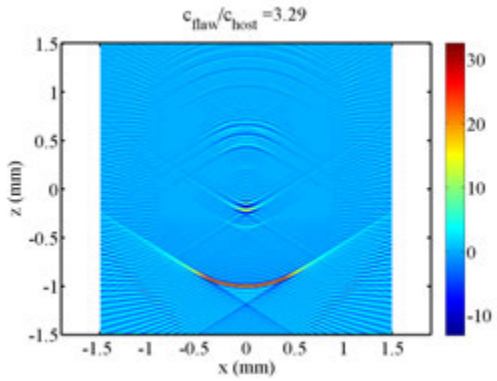

Figure B.13: $\frac{c_{flaw}}{c_{host}} = \frac{\rho_{flaw}}{\rho_{host}} = 3.29$

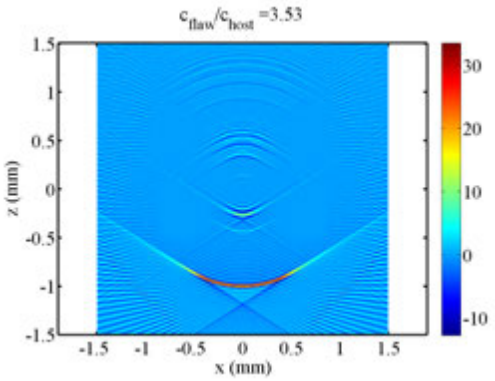

Figure B.14: $\frac{c_{flaw}}{c_{host}} = \frac{\rho_{flaw}}{\rho_{host}} = 3.53$

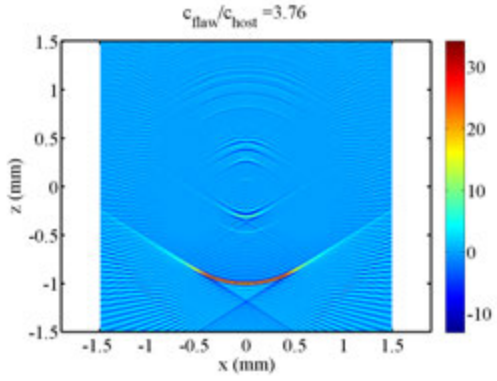

Figure B.15: $\frac{c_{flaw}}{c_{host}} = \frac{\rho_{flaw}}{\rho_{host}} = 3.76$

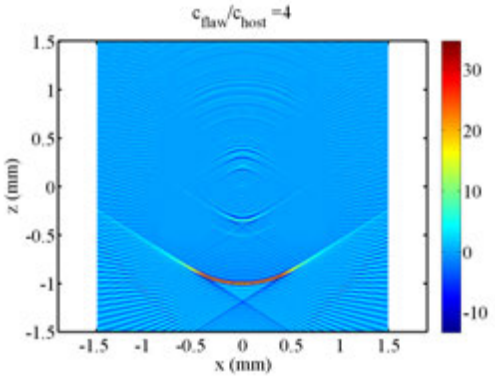

Figure B.16: $\frac{c_{flaw}}{c_{host}} = \frac{\rho_{flaw}}{\rho_{host}} = 4.00$

www.manaraa.com

BIBLIOGRAPHY

[1] P. N. Wells, "Ultrasonic imaging of the human body," *Reports on Progress in Physics*, vol. 62, no. 5, p. 671, 1999.

[2] L. W. Schmerr Jr, *Fundamentals of ultrasonic nondestructive evaluation: a modeling approach*. Plenum Press New York, 1998.

[3] J. P. Charlesworth and J. A. G. Temple, *Engineering applications of ultrasonic time-of-flight diffraction (2nd Ed.*, vol. 1. Research Studies Press Somerset, LTD, 2001.

[4] N. Bojarski, "A survey of the physical optics inverse scattering identity," *Antennas and Propagation, IEEE Transactions on*, vol. 30, no. 5, pp. 980–989, 1982.

[5] B. Kenzie and J. Speck, *Structural integrity with time of flight diffraction (TOFD) ultrasonic inspection*. http://www.twi.co.uk/technical-knowledge/published-papers /structural-integrity-with-time-of-flight-diffraction-tofd-ultrasonic-inspection-july-2005/. July 2005. Accessed: 04-05-2013.

[6] J. H. Rose, "Elastic wave inverse scattering in nondestructive evaluation," *Pure and Applied Geophysics*, vol. 131, no. 4, pp. 715–739, 1989.

[7] D. O. Thompson, S. J. Wormley, and D. K. Hsu, "Apparatus and technique for reconstruction of flaws using model-based elastic wave inverse ultrasonic scattering," *Review of scientific instruments*, vol. 57, no. 12, pp. 3089–3098, 1986.

[8] C.-P. Chiou and L. W. Schmerr Jr, "New approaches to model-based ultrasonic flaw sizing," *The Journal of the Acoustical Society of America*, vol. 92, p. 435, 1992.

www.manaraa.com

[9] C. Holmes, B. W. Drinkwater, and P. D. Wilcox, "Post-processing of the full matrix of ultrasonic transmit–receive array data for non-destructive evaluation," *NDT & E International*, vol. 38, no. 8, pp. 701–711, 2005.

[10] P. D. Wilcox, C. Holmes, and B. W. Drinkwater, "Advanced reflector characterization with ultrasonic phased arrays in nde applications," *Ultrasonics, Ferroelectrics and Frequency Control, IEEE Transactions on*, vol. 54, no. 8, pp. 1541–1550, 2007.

[11] D. Lévesque, A. Blouin, C. Neron, and J.-P. Monchalin, "Performance of laser-ultrasonic f-saft imaging," *Ultrasonics*, vol. 40, no. 10, pp. 1057–1063, 2002.

[12] P. D. Wilcox, C. Holmes, and B. W. Drinkwater, "Enhanced defect detection and characterisation by signal processing of ultrasonic array data," in *European Conference on Non-Destructive Testing*, 2006.

[13] M. Jobst and G. D. Connolly, "Demonstration of the application of the total focusing method to the inspection of steel welds," *European Conference on Non-Destructive Testing*, 2010.

[14] A. Velichko and P. D. Wilcox, "An analytical comparison of ultrasonic array imaging algorithms," *The Journal of the Acoustical Society of America*, vol. 127, p. 2377, 2010.

[15] J. Zhang, B. Drinkwater, and P. Wilcox, "Comparison of ultrasonic array imaging algorithms for non-destructive evaluation," in *Review of Progress in Quantitative Nondestructive Evaluation*, vol. 32, p. 825, 2013.

[16] P. D. Wilcox, "Ultrasonic arrays in nde: Beyond the b-scan," in *Review of Progress in Quantitative Nondestructive Evaluation*, vol. 32, p. 33, 2013.

[17] N. Bleistein, "Physical optics farfield inverse scattering in the time domain," *The Journal of the Acoustical Society of America*, vol. 60, p. 1249, 1976.

www.manaraa.com

[18] J. K. Cohen and N. Bleistein, "The singular function of a surface and physical optics inverse scattering," *Wave Motion*, vol. 1, no. 3, pp. 153–161, 1979.

[19] B. J. Engle, L. W. Schmerr Jr, and A. Sedov, "Equivalent flaw time-of-flight diffraction sizing with ultrasonic phased arrays," in *Review of Progress in Quantitative Nondestructive Evaluation*, vol. 32, p. 895, 2013.

[20] B. R. Titmann and N. E. Paton, "New ultrasonic standards," *Proceedings of the ARPA/AFML Review of Progress in Quantitative NDE*, pp. 331–335, 1978.

[21] C. C. Bampton, "Ultrasonic test samples," in *Review of Progress in Quantitative Nondestructive Evaluation* (D. O. Thompson and D. E. Chimenti, eds.), vol. 1, pp. 315–319, 1982.

[22] S.-J. Song and L. W. Schmerr, "An ultrasonic time-of-flight equivalent flaw sizing method," *Journal of Research in Nondestructive Evaluation*, vol. 4, no. 1, pp. 1–18, 1992.

[23] L. W. Schmerr Jr, B. J. Engle, A. Sedov, and X. Li, "Ultrasonic flaw sizing-an overview," in *Review of Progress in Quantitative Nondestructive Evaluation*, vol. 32, p. 1817, 2013.

[24] R. Thompson and T. Gray, "A model relating ultrasonic scattering measurements through liquid–solid interfaces to unbounded medium scattering amplitudes," *The Journal of the Acoustical Society of America*, vol. 74, pp. 1279–1290, 1983.

[25] L. W. Schmerr and S.-J. Song, *Ultrasonic nondestructive evaluation systems: models and measurements*. Springer, 2007.

[26] L. W. Schmerr Jr, "Fundamentals of ultrasonic phased arrays." Unpublished manuscript.

[27] W. Sachse and S. Golan, "The scattering of elastic pulses and the non-destructive evaluation of materials," *Elastic Waves and Non-Destructive Testing of Materials - American Society of Mechanical Engineers*, vol. 29, p. 11, 1978.

www.manaraa.com

[28] G. V. Frisk and H. Überall, “Creeping waves and lateral waves in acoustic scattering by large elastic cylinders,” *The Journal of the Acoustical Society of America*, vol. 59, p. 46, 1976.

www.manaraa.com